

JPL D-13407, Rev. A

## Multi-angle Imaging SpectroRadiometer (MISR)

# Experiment Overview

Approval:

David J. Diner  
MISR Principal Investigator

The MISR web site should be consulted to determine the latest released version of this document (<http://www-misr.jpl.nasa.gov>).  
Approval signatures are on file with the MISR Project.



**Jet Propulsion Laboratory**  
California Institute of Technology

## TABLE OF CONTENTS

<b>1. INTRODUCTION.....</b>	<b>1</b>
1.1 PURPOSE.....	1
1.2 SCOPE.....	1
1.3 MISR DOCUMENTS.....	1
1.4 REVISIONS .....	2
1.5 ACKNOWLEDGMENTS.....	2
<b>2. INSTRUMENT DESCRIPTION.....</b>	<b>3</b>
2.1 INSTRUMENT AND MEASUREMENT OVERVIEW .....	3
2.2 CAMERAS .....	4
2.3 STRUCTURAL DESIGN .....	5
2.4 ON-BOARD CALIBRATOR .....	5
2.4.1 Diffuse panels .....	5
2.4.2 Calibration photodiodes .....	5
2.4.3 Goniometer .....	6
2.5 OBSERVATIONAL CHARACTERISTICS .....	6
2.6 INSTRUMENT PERFORMANCE.....	7
<b>3. RADIANCE SCALING AND CONDITIONING .....</b>	<b>9</b>
3.1 OBJECTIVES .....	9
<b>4. GEORECTIFICATION AND REGISTRATION .....</b>	<b>11</b>
4.1 OBJECTIVES .....	11
4.2 USE OF SPACE-OBLIQUE MERCATOR PROJECTION.....	12
4.3 TERRAIN PROJECTION.....	12
4.4 ELLIPSOID PROJECTION .....	13
<b>5. AEROSOL RETRIEVALS .....</b>	<b>14</b>
5.1 OBJECTIVES .....	14
5.1.1 Aerosol climatic effects .....	14
5.1.2 Aerosol sources and sinks.....	15
5.1.3 Atmospheric corrections .....	15
5.2 HISTORICAL PERSPECTIVE.....	16
5.2.1 Current knowledge regarding tropospheric aerosols.....	16
5.2.2 Aerosol retrievals over dark water.....	17
5.2.3 Aerosol retrievals over land .....	18

5.3 BENEFITS OF MULTI-ANGLE VIEWING .....	18
6. SURFACE RETRIEVALS.....	20
6.1 OBJECTIVES .....	20
6.1.1 Surface radiative fluxes .....	21
6.1.2 Land surface classification .....	22
6.1.3 Ocean surface observations.....	22
6.2 HISTORICAL PERSPECTIVE.....	23
6.2.1 Land surface HDRF and BRF .....	24
6.2.2 Land surface BHR and DHR.....	24
6.2.3 Parametric models of bidirectional reflectance factor (BRF).....	25
6.2.4 Fractional absorbed photosynthetically active radiation (FPAR).....	27
6.2.5 Ocean surface equivalent reflectances .....	27
6.3 BENEFITS OF MULTI-ANGLE VIEWING .....	28
7. CLOUD STUDIES.....	31
7.1 OBJECTIVES.....	31
7.1.1 Cloud detection and screening.....	31
7.1.2 Cloud classification .....	33
7.1.3 Cloud climatic effects.....	34
7.1.3.1 Fine albedos .....	34
7.1.3.2 Coarse albedos .....	35
7.1.3.3 Angular integrations.....	35
7.2 HISTORICAL PERSPECTIVE.....	36
7.2.1 Cloud detection and screening.....	36
7.2.2 Cloud classification .....	36
7.2.2.1 Classification by elevation .....	37
7.2.2.2 Classification by angular signature .....	37
7.2.2.3 Classification by texture.....	38
7.2.3 Cloud climatic effects.....	38
7.3 BENEFITS OF MULTI-ANGLE VIEWING .....	39
8. DATA PRODUCTS .....	40
8.1 MISR SCIENCE DATA PROCESSING.....	40
8.2 TERMINOLOGY .....	41
8.3 PRODUCT SUMMARY .....	41
8.4 DATASET SUMMARY .....	43
9. DATA PRODUCT VALIDATION AND QUALITY ASSESSMENT.....	44

<b>9.1 VALIDATION .....</b>	<b>44</b>
<b>9.1.1 Aircraft instruments .....</b>	<b>44</b>
<b>9.1.2 Field measurements .....</b>	<b>45</b>
<b>9.2 QUALITY ASSESSMENT .....</b>	<b>45</b>
<b>9.2.1 Quality Assessment within the PGS software .....</b>	<b>45</b>
<b>9.2.2 Quality Assessment at the DAAC.....</b>	<b>46</b>
<b>9.2.3 Quality Assessment at the SCF .....</b>	<b>46</b>
<b>10. REFERENCES.....</b>	<b>47</b>

## **GLOSSARY OF ACRONYMS**

### **A**

ADM (Angular Distribution Model)  
AirMISR (Airborne MISR Simulator)  
ASAS (Advanced Solid-state Array Spectrometer)  
ASCM (Angular Signature Cloud Mask)  
ASTER (Advanced Spaceborne Thermal Emission and Reflectance radiometer)  
ATSR (Along-Track Scanning Radiometer)  
AVHRR (Advanced Very High Resolution Radiometer)  
AZM (Azimuthal Model)

### **B**

BDAS (Band-Differenced Angular Signature)  
BHR (Bi-hemispherical Reflectance)  
BRDF (Bidirectional Reflectance Distribution Function)  
BRF (Bidirectional Reflectance Factor)

### **C**

CCD (Charge-Coupled Device)  
CCN (Cloud Condensation Nuclei)  
CCS (Community Composition and Species)  
CERES (Clouds and the Earth's Radiant Energy System)  
ClearHC (Clear with High Confidence)  
ClearLC (Clear with Low Confidence)  
CloudHC (Cloud with High Confidence)  
CloudLC (Cloud with Low Confidence)  
CSSC (Cloud Screening Surface Classification)  
CZCS (Coastal Zone Color Scanner)

### **D**

DAAC (Distributed Active Archive Center)  
DDV (Dense Dark Vegetation)  
DEM (Digital Elevation Model)  
DHR (Directional-Hemispherical Reflectance)  
DN (Data Number)

### **E**

EOS (Earth Observing System)  
ERB (Earth Radiation Budget)  
ERBE (Earth Radiation Budget Experiment)  
ERBS (Earth Radiation Budget Satellite)

## **F**

FOV (Field of View)

FPAR (Fraction of Photosynthetically Active Radiation)

## **G**

GAC (Global Area Coverage)

GER (Geophysical Environmental Research)

GOES (Geostationary Operational Environmental Satellite)

## **H**

HDRF (Hemispherical-Directional Reflectance Factor)

HQE (High Quantum Efficiency)

## **I**

IAMAP (International Association for Meteorology and Atmospheric Physics)

IFOV (Instantaneous Field Of View)

IN (Ice Nuclei)

IR (Infrared)

## **M**

MFRSR (Multifilter Rotating Shadowband Radiometer)

MISR (Multi-angle Imaging SpectroRadiometer)

MKS (Meter, Kilogram, Second)

MODIS (Moderate Resolution Imaging Spectroradiometer)

## **N**

NOAA (National Oceanic and Atmospheric Administration)

## **O**

OBC (On-Board Calibrator)

## **P**

PAR (Photosynthetically Active Radiation)

PARABOLA (Portable Apparatus for Rapid Acquisition of Bidirectional Observations of the Land and Atmosphere)

PGS (Product Generation System)

PIN (p/intrinsic/n doped layers)

PSS (Primary Support Structure)

PTFE, polytetrafluoroethylene

## **Q**

QA (Quality Assessment)

QE (Quantum Efficiency)

## **R**

RCCM (Radiometric Camera-by-camera Cloud Mask)

RH (Relative Humidity)

RLRA (Reflecting Level Reference Altitude)

RMS (Root Mean Square)

RT (Radiative Transfer)

## **S**

SAGE (Stratospheric Aerosol and Gas Experiment)

SAM (Stratospheric Aerosol Monitor)

SCF (Science Computing Facility)

SDCM (Stereoscopically Derived Cloud Mask)

SeaWiFS (Sea-viewing, Wide-Field-of-View Sensor)

SERCAA (Support of Environmental Requirements for Cloud Analysis and Archive)

SI (Système International)

SMART (Simulated MISR Ancillary Radiative Transfer)

SNR (Signal-to-Noise Ratio)

SPOT (System Probatoire de l'Observation de la Terre)

## **T**

TASC (Terrestrial Atmosphere and Surface Climatology)

TEC (Thermo-Electric Cooler)

TOA (Top-of-Atmosphere)

TOAC (Tropical Ocean Atmospheric Correction)

## **W**

WCP (World Climate Programme)

WGS (World Geodetic System)

## **Y**

YES (Yankee Environmental Systems)

# 1. INTRODUCTION

## 1.1 PURPOSE

This Experiment Overview is generated in order to summarize in a single document high-level information about the Multi-angle Imaging SpectroRadiometer (MISR) instrument, measurement approach, science objectives, and data products. It also provides references to more detailed documentation on each of these topics.

## 1.2 SCOPE

Chapter 1 describes the purpose and scope of the document. A description of the MISR instrument is presented in Chapter 2. Radiometric and geometric processing objectives are discussed in Chapters 3 and 4. Chapters 5, 6, and 7 describe the MISR science objectives with regard to aerosols, surface, and clouds. A data product summary is presented in Chapter 8. Product validation and quality assessment is discussed in Chapter 9. Literature references used throughout the document are provided in Chapter 10. Within the text, these references are indicated by a number in italicized square brackets, e.g., [1].

## 1.3 MISR DOCUMENTS

References to MISR Project documents are indicated by a number in italicized square brackets as follows, e.g., [M-1]. The MISR web site (<http://www-misr.jpl.nasa.gov>) should be consulted to determine the latest released version of each of these documents.

[M-1] Data Product Description, JPL D-11103.

[M-2] Level 1 Radiance Scaling and Conditioning Algorithm Theoretical Basis, JPL D-11507.

[M-3] Level 1 Georectification and Registration Algorithm Theoretical Basis, JPL D-11532.

[M-4] Level 1 Cloud Detection Algorithm Theoretical Basis, JPL D-13397.

[M-5] Level 1 In-flight Radiometric Calibration and Characterization Algorithm Theoretical Basis, JPL D-13398.

[M-6] Level 1 Ancillary Geographic Product Algorithm Theoretical Basis, JPL D-13400.

[M-7] Level 1 In-flight Geometric Calibration Algorithm Theoretical Basis, JPL D-13399.



*[M-8]* Level 2 Cloud Detection and Classification Algorithm Theoretical Basis, JPL D-11399.

*[M-9]* Level 2 Top-of-Atmosphere Albedo Algorithm Theoretical Basis, JPL D-13401.

*[M-10]* Level 2 Aerosol Retrieval Algorithm Theoretical Basis, JPL D-11400.

*[M-11]* Level 2 Surface Retrieval Algorithm Theoretical Basis, JPL D-11401.

*[M-12]* Level 2 Ancillary Products and Datasets Algorithm Theoretical Basis, JPL D-13402.

*[M-13]* Algorithm Development Plan, JPL D-11220.

*[M-14]* In-flight Radiometric Calibration and Characterization Plan, JPL D-13315.

*[M-15]* In-flight Geometric Calibration Plan, JPL D-13228.

*[M-16]* Science Data Validation Plan, JPL D-12626.

*[M-17]* Science Data Quality Indicators, JPL D-13496.

## **1.4 REVISIONS**

This document will be updated as the experiment evolves, and as new information becomes available. Revisions from the previous version will be shown through the use of change bars. This revision, Rev. A, differs from the previous release in minor editorial updates only.

## **1.5 ACKNOWLEDGMENTS**

Many individuals contributed to the writing and concepts represented in this document. These include the members of the MISR Science Team: David J. Diner (Principal Investigator), Thomas P. Ackerman, Carol J. Bruegge, James E. Conel, Roger Davies, Siegfried A. W. Gerstl, Howard R. Gordon, Ralph A. Kahn, John V. Martonchik, Jan-Peter Muller, Ranga Myneni, Bernard Pinty, Piers J. Sellers, and Michel M. Verstraete. Additional written material was provided by Larry Di Girolamo and Veljko Jovanovic.

## 2. INSTRUMENT DESCRIPTION

### 2.1 INSTRUMENT AND MEASUREMENT OVERVIEW

An artist's rendering of the MISR instrument is shown in Figure 1. At the heart of the instrument is the optical bench, which contains nine pushbroom cameras. The cameras are arranged with one camera (designated An) pointing toward the nadir, one bank of four cameras (designated Af, Bf, Cf, and Df in order of increasing off-nadir angle) pointing in the forward direction, and one bank of four cameras (designated Aa, Ba, Ca, and Da) pointing in the aftward direction. Images are acquired with nominal view angles, relative to the surface reference ellipsoid, of 0°, 26.1°, 45.6°, 60.0°, and 70.5° for An, Af/Aa, Bf/Ba, Cf/Ca, and Df/Da, respectively. Each camera uses four Charge-Coupled Device (CCD) line arrays in a single focal plane. Each line array is filtered to provide one of four MISR spectral bands. The spectral band shapes are nominally gaussian, centered at 446, 558, 672, and 866 nm. A number of measurement objectives are established for the MISR experiment. The combinations of the 36 instrument channels (9 angles x 4 bands) used to meet these objectives are illustrated in Figure 2.

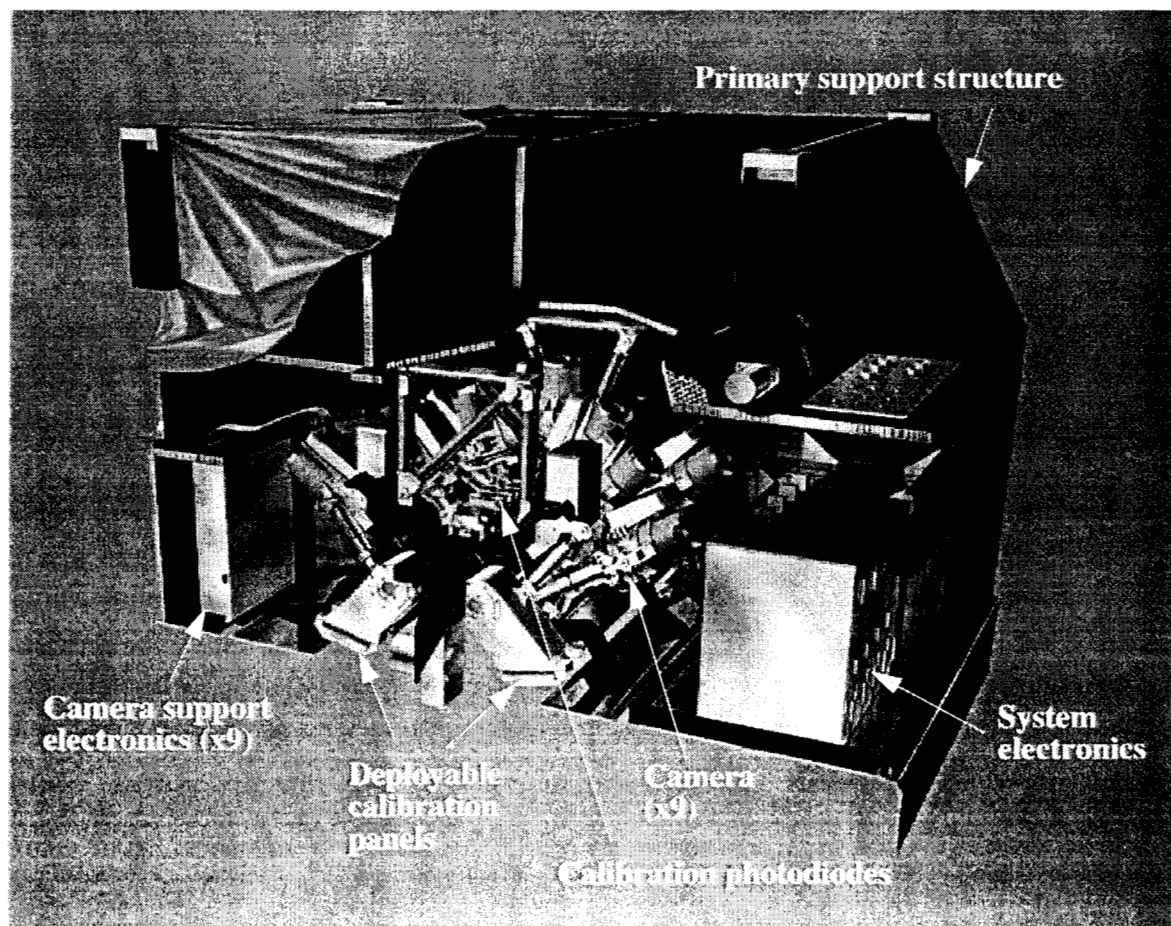
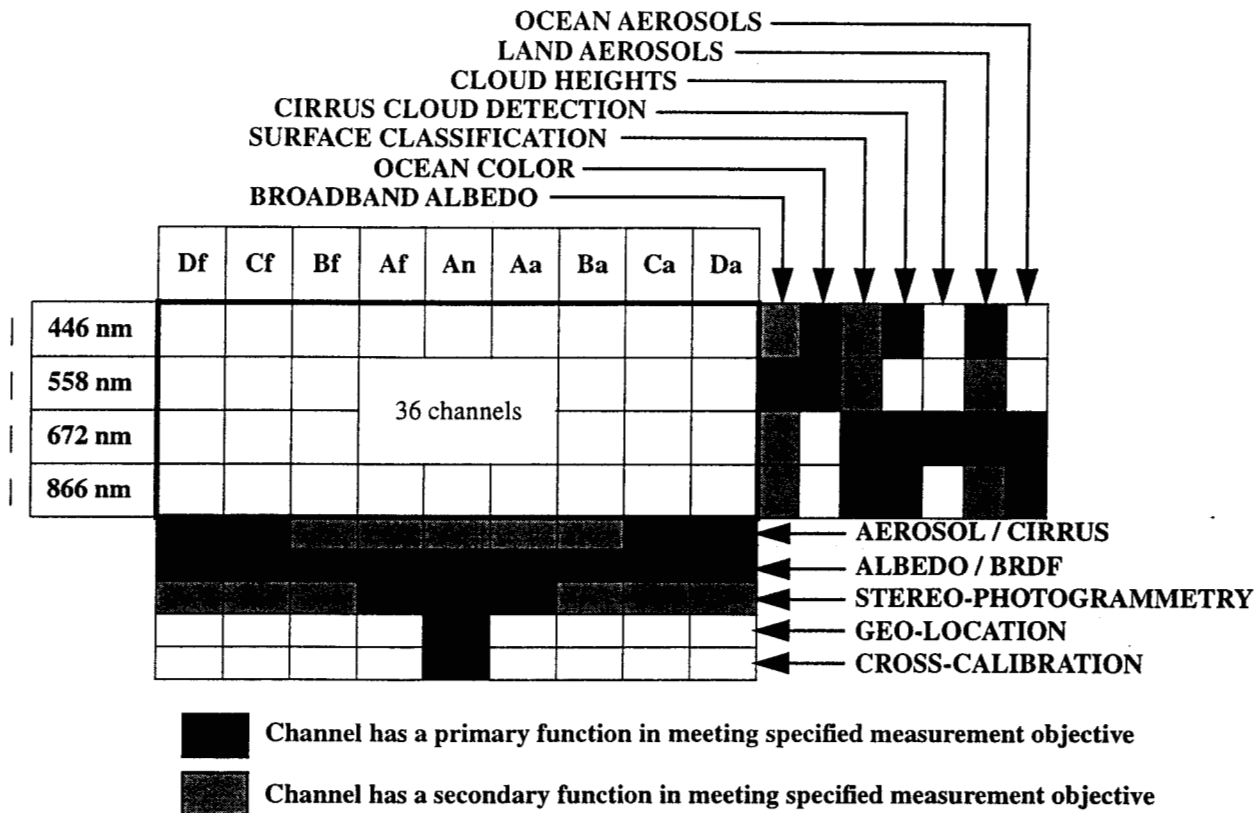


Figure 1. Artist's rendering of the MISR instrument



**Figure 2. Measurement objectives of MISR's nine cameras and four bands**

## 2.2 CAMERAS

The MISR lenses range in focal length from 59.3 mm to 123.8 mm and are superachromatic, 7-element refractive f/5.5 telecentric designs. A double plate Lyot depolarizer is incorporated into each of the cameras in order to render them polarization insensitive. The lenses are mounted in aluminum barrels with some additional materials to accommodate thermally induced dimensional changes of the lenses during flight. Each MISR camera contains a camera head which houses the focal plane structure and to which is attached the driver electronics for the CCD's. The camera heads and electronics are identical for all nine cameras, leading to a modular design in which only the lens barrels are unique.

MISR contains 36 parallel signal chains corresponding to the four spectral bands in each of the nine cameras. Each signal chain contains the output from the 1520 pixels (1504 photo-active plus 8 light-shielded plus 8 "overclock" samples of the CCD serial register) in each detector array. Each detector element measures 21  $\mu\text{m}$  (cross-track) by 18  $\mu\text{m}$  (along-track). The MISR CCD architecture is based on standard 3-phase, 3-poly, n-buried channel silicon detector technology. Thinning of the poly gate over the active pixels increases the detectors' quantum efficiency in the blue spectral region. Full well capacity is  $10^6$  electrons with read noise < 20 electrons, yielding a

large dynamic range for the devices. The signal chains amplify and convert the CCD video into 14 bit digital numbers, which are square-root encoded to 12 bits by the system electronics. To minimize dark current and radiation sensitivity, the CCD's are operated at  $-5^{\circ} \pm 0.1^{\circ}\text{C}$  using a single stage Thermo-Electric Cooler (TEC) in each focal plane.

A focal plane filter assembly defining the four optical bandpasses is placed about 1.5 mil above the CCD. The camera filters are mosaicked arrays of four separate medium band filters. Masks are placed over the epoxy bond lines between the different filters in order to prevent white light from leaking to the focal plane. The filters use ion assisted deposition technology to insure stable and durable coatings which will not shift or degrade with age or environmental stresses.

## **2.3 STRUCTURAL DESIGN**

The MISR instrument configuration includes the optical bench and the primary support structure (PSS). The optical bench holds the nine cameras at their light-admitting end with the detector end cantilevered into the instrument cavity. The fore-aft cameras are paired in a symmetrical arrangement and set at fixed view angles on the optical bench. In addition to the cameras, the optical bench contains calibration hardware, described in the next section. The PSS provides kinematic attachment to the spacecraft bus and is designed to maintain rigid support for the optical bench. The instrument enclosure provides a structural mount for the nadir-facing radiators. In addition, it houses the optical bench assembly, the instrument system electronics, and the flight computer.

## **2.4 ON-BOARD CALIBRATOR**

### **2.4.1 Diffuse panels**

A key component of the MISR On-Board Calibrator (OBC) is a pair of deployable diffuse panels. These are covered with Spectralon, a pure polytetrafluoroethylene (PTFE, or Teflon) polymer resin which is compressed and sintered. While not in use the panels are stowed and protected. At approximately monthly intervals the panels are deployed for calibration. Over the North Pole, a panel will swing aftward to diffusely reflect sunlight into the fields-of-view of the aftward-looking and nadir cameras. Over the South Pole, the other panel will swing forward for calibration of the forward-looking and nadir cameras. The nadir camera will provide a link between the two sets of observations.

### **2.4.2 Calibration photodiodes**

The diffuse calibration targets are monitored in-flight by three types of diodes: radiation-resistant PIN photodiodes and two types of high quantum efficiency (HQE) diodes. (Note "PIN" is a description of the diode architecture where *p*, intrinsic, and *n* doped layers are stacked.) The radiation-resistant photodiodes are fabricated four to a package, each diode filtered to a different

MISR spectral band. Five such packages will be used. Two will view in the nadir direction, two in the Df and Da camera directions, and one package will be mechanized on a goniometric arm to monitor the angular reflectance properties of the panels.

The HQE's are in a "trap" configuration. Here three silicon photodiodes are arranged in a package so that light reflected from one diode is absorbed by another diode. The output of each diode is summed in parallel, resulting in near 100% quantum efficiency. A single spectral filter per package is used, and four such packages provide coverage at the four MISR wavelengths. One diode type will be used to obtain high quantum efficiency (QE) in the blue (first two spectral bands), and another type will be optimized for QE in the red and near-IR (last two MISR spectral bands).

### **2.4.3 Goniometer**

The goniometer is a device that characterizes the relative diffuse panel radiance function with angle. It does so in a plane parallel to the spacecraft flight direction. A PIN package mounted to the goniometer arm swings through  $\pm 60^\circ$  to allow panel characterization appropriate to the downtrack camera angles.

## **2.5 OBSERVATIONAL CHARACTERISTICS**

From the 705-km descending polar orbit of the EOS-AM spacecraft, the zonal overlap swath width of the MISR imaging data (that is, the swath seen in common by all nine cameras along a line of constant latitude) is 360 km, which provides global multi-angle coverage of the entire Earth in 9 days at the equator, and 2 days at the poles. The crosstrack IFOV and sample spacing of each pixel is 275 m for all of the off-nadir cameras, and 250 m for the nadir camera. Downtrack IFOV's depend on view angle, ranging from 214 m in the nadir to 707 m at the most oblique angle. Sample spacing in the downtrack direction is 275 m in all cameras. The instrument is capable of buffering the data to provide 2 sample x 2 line, 4 sample x 4 line, or 1 sample x 4 line averages, in addition to the mode in which pixels are sent with no averaging. The averaging capability is individually selectable within each of the 36 channels.

There are several observational modes of the MISR instrument. Global Mode refers to continuous operation with no limitation on swath length. Global coverage in a particular spectral band of one camera is provided by operating the corresponding signal chain continuously in a selected resolution mode. Any choice of averaging modes among the nine cameras that is consistent with the instrument power and data rate allocation is suitable for Global Mode. Additionally, Local Mode provides high resolution images in all 4 bands of all 9 cameras for selected Earth targets. This is accomplished by inhibiting pixel averaging in all bands of each of the cameras in sequence, one at a time, beginning with the first camera to acquire the target and ending with the last camera to view the target. The instrument geometry limits the downtrack length of Local Mode targets to about 300 km. Finally, in Calibration Mode the on-board calibration hardware is deployed and cal-

ibration data are acquired for the cameras. Calibration data will be obtained for each spatial sampling mode (see above) by cycling each channel through the various modes during the calibration period. Calibration Mode will be used on a monthly basis during routine mission operations, although early in the mission it will be used more frequently.

The MISR standard products are generated from Global Mode data. Current plans are to acquire global data sets by operating the instrument in the 4 x 4 averaging mode (1.1-km sampling), with selected channels operated in either 1 x 1 or 1 x 4 mode.

## 2.6 INSTRUMENT PERFORMANCE

The quality of MISR geophysical retrievals is a function of the signal-to-noise ratio (SNR) performance of the instrument. Radiometric requirements on the MISR instrument are defined at signal levels expressed as equivalent reflectances,  $\rho_{equiv}$ . Equivalent reflectance is defined as:

$$\rho_{equiv} = \pi L_{\lambda} / E_{0\lambda} \quad (1)$$

where  $L_{\lambda}$  is the spectral radiance incident at the sensor, and  $E_{0\lambda}$  is the spectral exo-atmospheric solar irradiance at wavelength  $\lambda$ . The use of equivalent reflectance permits the radiance levels at which radiometric requirements are specified in all spectral bands to be expressed in terms of a single band-independent parameter. Equivalent reflectance conceptually represents an arbitrary radiance level in terms of the particular value of reflectance of an exo-atmospheric lambertian target, illuminated by the Sun at normal incidence, that would yield the same radiance at the sensor. For example, a perfectly reflecting lambertian target illuminated by overhead Sun has a true reflectance and an equivalent reflectance of 100% at all view angles. If the same target were illuminated at a solar incidence angle of 60°, its true reflectance remains 100%, but the radiometric equivalent reflectance would be 50% ( $\cos 60^{\circ} \times 100\%$ ) at all view angles.

Typical SNR's for the MISR instrument based on preflight testing is shown as a function of equivalent reflectance in Table 1. The linear encoding of MISR data to 14 bits, followed by square-root encoding to 12 bits, provides for a very high dynamic range in the instrument. Values are presented for both unaveraged data and for data which has been subjected to 4 sample x 4 line averaging within the instrument.

**Table 1: MISR signal-to-noise ratios**

Equivalent reflectance	Averaging mode 1x1	Averaging mode 4x4
1.00	986	3944
0.70	824	3296
0.50	695	2780
0.20	436	1744
0.15	376	1504
0.10	305	1220
0.07	253	1012
0.05	210	840
0.03	158	632
0.02	125	500
0.01	80	320
0.007	62	248
0.005	48	192
0.002	23	92
0.001	12	48

### 3. RADIANCE SCALING AND CONDITIONING

#### 3.1 OBJECTIVES

The only directly measured physical parameters observed by MISR are camera incident radiances. Geophysical parameters are derived from these data. Yet, the data numbers (DN) transmitted by MISR only provide an accurate measure of these radiances once a series of processing steps, called radiance scaling and conditioning, have been performed. During radiance scaling the DN values are converted to spectral radiances, and reported in MKS (Meter, Kilogram, Second) units referred to as SI (Système International). Use is made of camera calibration coefficients, relating the response of the system to a known radiance field, as determined through many different activities conducted both preflight and in-flight. These coefficients will be updated monthly, and stored in an archived dataset known as the Ancillary Radiometric Product [M-5]. The in-flight calibration will be accomplished through the use of the On-Board Calibrator, vicarious calibrations conducted during field experiments performed simultaneously with EOS-AM overflights, instrument performance trend analyses, and histogram equalization techniques utilizing Earth scene data. Independent verifications will be made using cross-comparisons with targets viewed in common with the Moderate Resolution Imaging Spectroradiometer (MODIS).

Radiometric uncertainties for MISR are specified at the 68% confidence level (i.e.,  $1\sigma$ ). Table 3 shows the absolute and relative radiometric performance specifications for uniform targets of the indicated equivalent reflectances. Pixel-to-pixel uncertainties refer to the calibrated radiances from all pixels within a given detector array. Band-to-band uncertainties refer to the calibrated radiances from all pixels within a given camera, assumed to be illuminated by a target with the same equivalent reflectance in all bands. Camera-to-camera uncertainties refer to the calibrated radiance values derived from all pixels within all cameras, within a given spectral band, and determine the ability to distinguish angular shapes of TOA radiance fields. Not all of the MISR measurement objectives are dependent upon high absolute accuracies. For example, the determination of the shape of angular reflectance signatures of surfaces and clouds are dependent only on the relative camera-to-camera and band-to-band radiometric accuracy. The requirements for these calibrations are such that sufficient accuracy is achieved for studies making use of directional reflectances.

**Table 2: Limits on required radiometric uncertainty**

<b>Equivalent reflectance</b>	<b>Maximum absolute radiometric uncertainty</b>	<b>Maximum pixel-to-pixel radiometric uncertainty</b>	<b>Maximum band-to-band radiometric uncertainty</b>	<b>Maximum camera-to-camera radiometric uncertainty</b>
100%	$\pm 3.0\%$	$\pm 0.5\%$	$\pm 1.0\%$	$\pm 1.0\%$
5%	$\pm 6.0\%$	$\pm 1.0\%$	$\pm 2.0\%$	$\pm 2.0\%$



During ground data product generation, radiance scaling is performed in conjunction with another process called radiance conditioning. This is needed to compensate for imperfections in the instrument hardware. For example, requirements on the instrument radiometric performance over heterogeneous targets have been specified in order to minimize errors in aerosol characteristics derived from the radiance above dark targets (such as lakes) surrounded by brighter land, and to minimize contamination of radiances over large dark expanses, such as the ocean surface, by nearby bright objects (such as clouds). Camera testing has indicated that scattering between the filter and CCD in the camera focal planes results in low intensity “halos” around the camera point spread functions, causing the contrast target specifications to be violated. Deconvolution of the data during ground processing is capable of correcting for this effect. Other instrument corrections to be implemented include compensation for pixel-to-pixel gain non-uniformities, which affect the accuracy of instrument-averaged data (i.e.,  $1 \times 4$  or  $4 \times 4$ ) over heterogeneous targets; correction for imperfect out-of-band spectral rejection; and spurious signals in the CCD serial registers.

Details of the radiance scaling and conditioning algorithms are described in [M-2].

## 4. GEORECTIFICATION AND REGISTRATION

### 4.1 OBJECTIVES

After the reformatting of the raw instrument data and the conversion of DN to radiance, there is one remaining task before MISR science retrievals can be performed. This is the correction for geometric distortions inherent in the raw data and the georectification of the data from the nine camera views to a common projection. Geometric registration of the 36 channels of data from the instrument is also an essential requirement of the subsequent geophysical retrievals. The specific requirements are shown in Table 3. These are specified at a confidence level of 95%. The requirements insure accurate placement of MISR data products on a geographical grid and the ability to separate actual temporal changes on the Earth from misregistration errors. Registration of the data at these levels is driven primarily by the aerosol and surface retrievals, but is also necessary for the cloud retrievals in order to guarantee input of high geometric fidelity. The image geolocation and registration requirements specified apply to the data in all four spectral bands of each camera for which the requirement applies. Since the instrument acquires multi-spectral images with a spatial displacement between spectral bands, this displacement must be removed in the ground data processing.

**Table 3: Limits on required geometric uncertainty**

Category	Terrain-projected	Ellipsoid-projected
Along-track geolocation of nadir imagery (all bands)	$\pm 275$ m	$\pm 250$ m
Cross-track geolocation of nadir imagery (all bands)	$\pm 275$ m	$\pm 250$ m
Along-track registration (all channels)	$\pm 550$ m	$\pm 500$ m
Cross-track registration (all channels)	$\pm 275$ m	$\pm 250$ m

In photogrammetry, geometric distortions are defined as those errors which affect the ability to determine the geolocation of an individual pixel. Geometric distortions in remotely-sensed satellite imagery can be categorized as either internal (instrument-related) or external (spacecraft perturbations and viewing geometry). For the MISR instrument, most internal geometric distortions will be accounted for by extensive pre-flight geometric camera calibration. This calibration will consist of field-of-view mapping tests with camera subassemblies (optics and detectors) under thermal-vacuum conditions, and ambient testing of the cameras integrated into the optical bench. However, these ground tests do not include the effects of launch, gravity release, deformations of the mechanical connections between the optical bench and the satellite platform, and other possible sources. The effects of these variables on pointing can only be determined by in-flight geometric calibration. The results of pre-flight and in-flight calibration will be used to construct a camera model, which utilizes the rigid relation between the cameras, to describe the instrument pointing

in terms of static and dynamic (temperature dependent) parameters.

The primary source of external geometric errors is the position and pointing knowledge of the EOS-AM spacecraft. The specifications for the spacecraft are too large to meet the MISR science requirements for geolocation and registration. However, the spacecraft and instrument pointing is expected to be stable within a single orbit. In addition, the sun-synchronous nature of the orbit is expected to result in small orbit-to-orbit variations at the same location within the orbit. This high degree of stability and repeatability is factored into the georectification algorithm strategy.

## **4.2 USE OF SPACE-OBLIQUE MERCATOR PROJECTION**

By establishing a common map projection, or grid, for the geo-rectified radiances, a basis for the geophysical retrieval algorithms is formed, as required to account for the manner in which the instrument acquires the data and the algorithms need to utilize these data. Space-Oblique Mercator (SOM) is used for this grid because it minimizes distortion and resampling effects, since its projection meridian nominally follows the spacecraft ground track and a constant distance scale is preserved along that track. The map resolution of the projection will also be matched to the horizontal sampling mode of each camera channel. The horizontal datum for each projection is the World Geodetic System 1984 (WGS84) ellipsoid. The predetermined SOM grid is thereby an intermediate step to the Earth-based map projections to be used at higher processing levels when global mapping is to be performed. Because the SOM projection minimizes distortions and resampling effects, it permits the greatest flexibility in the choice of the Earth-based projections to be used. In addition, the map projection allows direct cross-comparison with data from other instruments and simplifies global mapping, since the data have already been geolocated.

A separate projection will be established for each of the paths of the 233 repeat orbits of the EOS 16-day cycle. Since each of the orbit paths repeat, the projection grid for each path can be calculated only after the orbit is determined. The projection grid is then stored and used routinely for all successive cycles. This grid will be established by the Ancillary Geographic Product, which exists as separate, archived, supporting dataset [M-6].

## **4.3 TERRAIN PROJECTION**

Certain algorithms within the aerosol, surface, and cloud retrievals require the radiances from all nine cameras of MISR to be co-registered and projected to the surface terrain using a common projection system, which ensures that the same surface boundary condition applies to each of the nine views. In order to achieve this, it is necessary to correct for topographically-induced misregistration, and this is achieved by projecting the images to a surface defined by a digital elevation model (DEM). That is, the topographic errors due to the perspective viewing geometry of the nadir and off-nadir cameras and the band displacement within each camera are accounted for. Topographic errors are particularly sensitive to position and pointing knowledge, especially at the ex-

treme viewing angles of the MISR instrument.

In areas where it is necessary to correct for topography, the position and pointing information contained in the spacecraft ancillary data may not be adequate, on its own, for ground location of the MISR images. Therefore the MISR terrain projection algorithm will utilize matching to a set of reference images to supplement the spacecraft navigation data. This is done in an adaptive manner, i.e., it impacts the processing only where there is a significant ground location error from the supplied navigation data. In this matching scheme, the MISR image from each camera is registered to a set of reference orbit imagery, there being one set of nine for the respective nine cameras, and 233 sets corresponding to the 233 unique orbits in a 16-day cycle. The reference orbit imagery is constructed from MISR data collected early in the EOS-AM mission, and chosen to be relatively cloud-free. Because the EOS-AM spacecraft is highly stable, it will not matter if significant portions of the reference orbit images are cloud-covered. In cases where reference imagery is not yet available, the algorithm will operate with the accuracy corresponding to the spacecraft-supplied navigation alone. In addition, for cloudy or featureless scenes (e.g., ocean) no matching will be performed and the navigation will be used as reported; however, static corrections obtained from matching in other regions are applied.

Following the ground location through image matching or simple use of the navigation ancillary data, each MISR image is modified using a set of projection parameters to achieve the resampling necessary to ortho-rectify the image to the SOM grid. For further information, see [M-3].

#### **4.4 ELLIPSOID PROJECTION**

Certain algorithms within the top-of-atmosphere/cloud retrievals require the radiances from all nine cameras of MISR to be additionally projected to a surface defined by the WGS84 ellipsoid. For example, this surface is where camera-to-camera stereo matching will be performed to determine cloud altitude. Projection of the imagery from the nine cameras (and individual bands) to a smooth ellipsoid is not as sensitive to viewing geometry as is true for the terrain-projection algorithm. Therefore the spacecraft attitude and position is used as reported (but improved by the calibrated camera model and static corrections obtained from matching) to determine an intersection with the surface ellipsoid. Then, resampling of the imagery to the SOM projection is performed.

## 5. AEROSOL RETRIEVALS

### 5.1 OBJECTIVES

Aerosols are solid or liquid airborne particulates of various compositions, frequently found in stratified layers. Generally, they are defined as atmospheric particles with sizes between about 0.1  $\mu\text{m}$  and 10  $\mu\text{m}$ , though the sizes of condensation nuclei are typically about 0.01  $\mu\text{m}$ . Under normal conditions, most of the atmospheric aerosol resides in the troposphere. Natural sources (e.g., dust storms, desert and soil erosion, biogenic emissions, forest and grassland fires, and sea spray) account for about 90% of this aerosol, with the rest resulting from anthropogenic activity [137]. The background tropospheric aerosol is temporally and spatially variable. The typical optical depth of this aerosol is  $\sim 0.1$  at visible wavelengths [123], though observational evidence [92], [111] suggests an increase in the tropospheric aerosol burden at mid-latitudes and in the Arctic, probably as the result of anthropogenic activities.

The overall scientific objectives of the MISR aerosol retrievals are:

- (1) To study, on a global basis, the magnitude and natural variability in space and time of sunlight absorption and scattering by aerosols in the Earth's atmosphere, particularly tropospheric aerosols, which is an important part of understanding their effect on climate;
- (2) To improve our knowledge of the sources, sinks, and global budgets of aerosols;
- (3) To provide atmospheric correction inputs for surface imaging data acquired by MISR and other instruments (e.g., MODIS and ASTER) that are simultaneously viewing the same portion of the Earth, for the purpose of making better quantitative estimates of surface reflectance.

Further background on each of these objectives is presented below.

#### 5.1.1 Aerosol climatic effects

Aerosols are thought to play a direct role in the radiation budget of Earth, on regional and hemispheric length scales [8], [65]; however, their net radiative effect, i.e., whether they heat or cool the surface, depends on their optical properties and the albedo of the underlying surface. For example, surface radiation measurements show that aerosols over the Eastern U.S. cause an average 7% reduction in insolation [120], whereas measurements of the absorption of solar radiation by pollutant haze in the Arctic atmosphere [128] show a clear increase in the amount of solar energy deposition. It is believed that on the global average, aerosols provide a net cooling effect. Northern hemispheric sources are believed to be sufficiently large so that the net radiative effect of anthropogenic sulfate aerosols alone is comparable in size (of order 1 - 2  $\text{W/m}^2$ ), though opposite in sign, to the anthropogenic  $\text{CO}_2$  radiative forcing [7].

Aerosols may also play an indirect role in the Earth's radiation balance, through their effects on clouds [129]. They serve as cloud condensation nuclei (CCN) and ice nuclei (IN), and their properties (concentration, size distribution, and composition) can affect the reflectivity, absorptivity, and lifetimes of clouds. In particular, an increase in CCN or IN is thought to increase the number of cloud particles, and for fixed cloud water content, will increase the net reflectivity (the "Twomey effect" [127]) and cloud lifetime (the "cloudiness effect"). Satellite observations of ship tracks in marine stratus show an increase in brightness in the solar infrared [13], lending support to this view. However, the CCN may also increase the cloud absorptivity [118], especially if they are soot particles or other dark material, and they may initiate precipitation. A calculation of the possible influence of a 30% increase in CCN on a 25% global marine stratocumulus cover produced an effective global albedo change on order 2% [6], amounting to a net radiative effect of 2 - 3 W/m<sup>2</sup>.

### 5.1.2 Aerosol sources and sinks

The lifetimes of tropospheric aerosol particles are thought to range from about a week to a little over a month. These include sulfuric acid particles, which form photochemically from SO<sub>2</sub> [126]. Because these lifetimes are short relative to global atmospheric mixing times, spatial-temporal patterns are often indicative of sources and sinks. For example, particles off the northwest coast of Africa and the east coast of central Asia are generally interpreted as being desert dust, those around Latin America in northern spring as forest fire particles, and those off the east coasts of Japan and North America as industrial particles [56]. However, current retrievals from AVHRR [99] are otherwise unable to distinguish different particle types or compositions, since they are based on measurements at a single wavelength and angle of view, and the algorithm to convert observed radiance to aerosol optical depth assumes particles of a fixed composition and size. MISR provides more extensive coverage in both wavelength and view angle, providing greater ability to distinguish different particle types based on their physical and optical properties. This will improve our ability to constrain the underlying sources, and to varying degrees, sinks and lifetimes, that govern their concentration in the troposphere.

### 5.1.3 Atmospheric corrections

The goal of any atmospheric correction scheme is the retrieval of surface reflectance or surface-leaving radiance from top-of-atmosphere (TOA) radiances. It is well established that scattering and absorption by aerosols are responsible for dramatic modifications of the spectral content of remotely sensed images of the Earth's surface, leading to classification errors [29], reduced accuracy of image products such as vegetation maps [55], and a degradation in the accuracy of quantitative estimates of surface radiative properties. The retrieval of aerosol scattering properties with MISR is an essential precursor to atmospheric correction of surface parameters [M-11].

## 5.2 HISTORICAL PERSPECTIVE

### 5.2.1 Current knowledge regarding tropospheric aerosols

In general, much less is known about tropospheric aerosols than stratospheric aerosols. The reasons for this are: (1) the stratospheric aerosol population is stable in space and time whereas in the troposphere, there are more known sources, more types of aerosols, and the lifetimes are short due to precipitation; (2) it is easier to measure stratospheric aerosols on a global scale from space with limb observing instruments such as SAM II and SAGE II. Aerosol optical depths, as well as spatial and temporal variability, make such observations in the troposphere more difficult and less likely to be representative; and (3) the ozone issue, and particularly the Antarctic ozone “hole,” has focused interest on stratospheric aerosols for their part in the heterogeneous chemistry of ozone. There are presently no universally accepted methods for retrieval of tropospheric aerosol properties from satellites, and algorithms to be used in processing of MISR data will be breaking new ground in this arena.

In order to constrain the MISR aerosol retrievals, it is advantageous to make reasonable use of what is known about the types of aerosols that are found in the troposphere. In general, tropospheric aerosols fall into a small number of compositional categories, which include sea spray, sulfate/nitrate, mineral dust, biogenic particles, and urban soot. Approximate size ranges, and the proclivity of each particle type to adsorb water under increasing relative humidity are also known. Therefore, the MISR team has chosen an approach in which the physical and chemical (and therefore optical) properties of candidate aerosols are completely prescribed. The advantages of this approach, in contrast to a purely “generic” representation in terms of effective single scattering albedo, effective size distribution, and effective phase function, are that it potentially enables identification of aerosol sources and provides the means of extending aerosol properties retrieved at the MISR wavelengths to other spectral regions, which will be useful for comparisons with other sensors and for model validation. To this end, a review of published aerosol climatologies was performed (in particular, [15], [71], [113], [138]). Certain aerosol attributes as described in these and other references (such as compositional and size classes) are adopted in the MISR retrievals. However, other attributes, such as specific spatial and temporal distributions are not assumed.

A summary of the MISR aerosol retrieval strategy is as follows: Based on the establishment of an aerosol climatology incorporating datasets describing the physical and compositional properties of specified mixtures of known types of aerosols, forward radiative transfer calculations are performed to provide various components of the atmospheric radiation field in the 36 MISR channels. During routine processing, these calculations will be binned into models that are observationally distinguishable by MISR. The pre-calculated results will be used in conjunction with the MISR observations to determine those models that provide good fits to the data, and to retrieve aerosol optical depth.

### 5.2.2 Aerosol retrievals over dark water

Because of the reflectance uniformity of the large water bodies (e.g., the ocean), and the fact that deep water bodies are essentially black at red and near-infrared wavelengths, considerably more progress has been made in development of algorithms to retrieve aerosol properties over dark water. Under the assumption of an aerosol model (i.e., specification of particle size distribution, particle shape, and complex refractive index), it is possible using radiative transfer (RT) theory to derive a one-to-one relationship between observed radiance and aerosol optical depth. Such modeling has been applied to the retrieval of aerosol concentration from Landsat [28], [45] and NOAA AVHRR [46], [76], [99], [119].

The AVHRR aerosol data set [76], [119] provides daily estimates of aerosol optical depth over ocean. The data set is global, covering between  $\pm 70^\circ$  latitude. Since June, 1989 results have been reported weekly and monthly at  $1^\circ$  spatial resolution. The retrievals provide an effective column optical depth adjusted to  $0.5 \mu\text{m}$  wavelength, based upon the assumption of spherical particles with  $n = 1.5 - 0.0i$  ("sulfate" composition), a specific Junge distribution of sizes, and an assumed lambertian surface of reflectivity 0.015. The AVHRR technique uses both visible reflectance over the ocean and error in derived sea-surface temperature (derived from infrared channels) to eliminate "cloud contaminated" areas when estimating aerosol optical thickness. Based on data from July 1989 to June 1991, zonal average background tropospheric aerosol levels over ocean were estimated to be about 0.15 in the northern hemisphere tropics, 0.10 in the subtropics, and 0.05 at higher latitudes. Regionally, the reported total aerosol column optical depth ranges from below  $10^{-2}$  (limit of detectability) to as large as 2.0. The northern tropical maximum in optical depth is attributed to Sahara dust over the Atlantic. A smaller, late-summer increase in northern mid-latitudes is attributed to dust from the Gobi desert blown eastward over the Pacific [56]. Other areas of interest include Latin America, where the surrounding water, east and west, shows increased aerosol optical depth in the spring. Rao et al. [99] associate the observation with slash-and-burn forest management at this time of year.

AVHRR sensitivity to optical depth (RMS error) is reported to be about 0.04; however this does not necessarily provide a measure of accuracy because it does not include systematic biases due to the particular model assumed in the retrieval [58]. For example, even for spherical particles with a known size distribution, an error as much as a factor of two could occur in the retrieved optical depth if the real part of the refractive index is assumed to be 1.55 when the correct index is 1.33. Substantial improvements in the retrieval of aerosol over ocean and other dark water bodies are possible with MISR. For marine aerosols, the scattering phase function depends only weakly on wavelength,  $\lambda$ , and the radiance backscattered out of the ocean can be estimated [39] with sufficient accuracy at  $\lambda > 500 \text{ nm}$  to determine the relative spectral variation of optical depth. This, in turn, provides a good estimate of the gross features of the aerosol size distribution [41]. Along with multi-angle radiances, which are governed strongly by the shape of the aerosol scattering phase functions, these measurements will provide additional information with which to refine the aerosol



model used in the retrieval of optical depth.

### 5.2.3 Aerosol retrievals over land

The retrieval of aerosol optical depth over land from space is considerably less well developed than the dark water case because of the higher brightness and heterogeneity of the land surface. As a consequence, separation of the land-leaving and atmosphere-leaving signals in remotely sensed radiances must be performed in order to retrieve aerosol properties from the measured signal. This is an active area of remote sensing research, particularly by the MODIS and MISR teams.

The simplest means of determining the atmospheric contribution to the satellite signal is to make an assumption about the surface reflectivity or albedo. An empirical method in which surface reflectivity was assumed to be known at a few points in a Landsat image was used for the purpose of removing atmospheric effects from the imagery [82]. The problem with this approach for global imaging is that the surface boundary condition is known only for selected points on the Earth. Locations where the surface boundary condition is believed to be reasonably well understood are areas covered by Dense Dark Vegetation (DDV). A method based on imaging over DDV has been investigated [63] and forms the basis of the MODIS aerosol retrieval over land [69]. The low reflectance of dense vegetation in the visible portion of the spectrum is used in conjunction with an aerosol model to retrieve optical depth. This approach is similar to the method used for retrievals over dark water. Therefore, MISR can provide enhancements analogous to those envisioned for dark water aerosol retrievals.

Since dense vegetation is found only over a portion of the land surface, other methods will be required to extend the aerosol retrieval spatial coverage. Separability of the surface-leaving and atmosphere-leaving signals over terrain with heterogeneous surface reflectance is the objective of several methods being explored by the MISR team [26], [81]. These new methods are tailored to the characteristics of the MISR observations, and there is little historical precedent for them. These approaches are discussed in [M-10].

## 5.3 BENEFITS OF MULTI-ANGLE VIEWING

The multi-angle viewing strategy of MISR provides information about aerosols in two principal ways:

- (1) The oblique viewing angles accentuate the aerosol signal because of the increased optical path length through the atmosphere.
- (2) The nine cameras provide coverage in scattering angle,  $\Omega$  (the angle between the direction of the Sun's rays and the direction to the sensor). The aerosol phase function, which is dependent on scattering angle, differs among aerosols of varying compositions and sizes.

Figure 3 shows the scattering angle coverage obtained across the fields-of-view of MISR's nine cameras as a function of latitude on the vernal equinox (March 21).

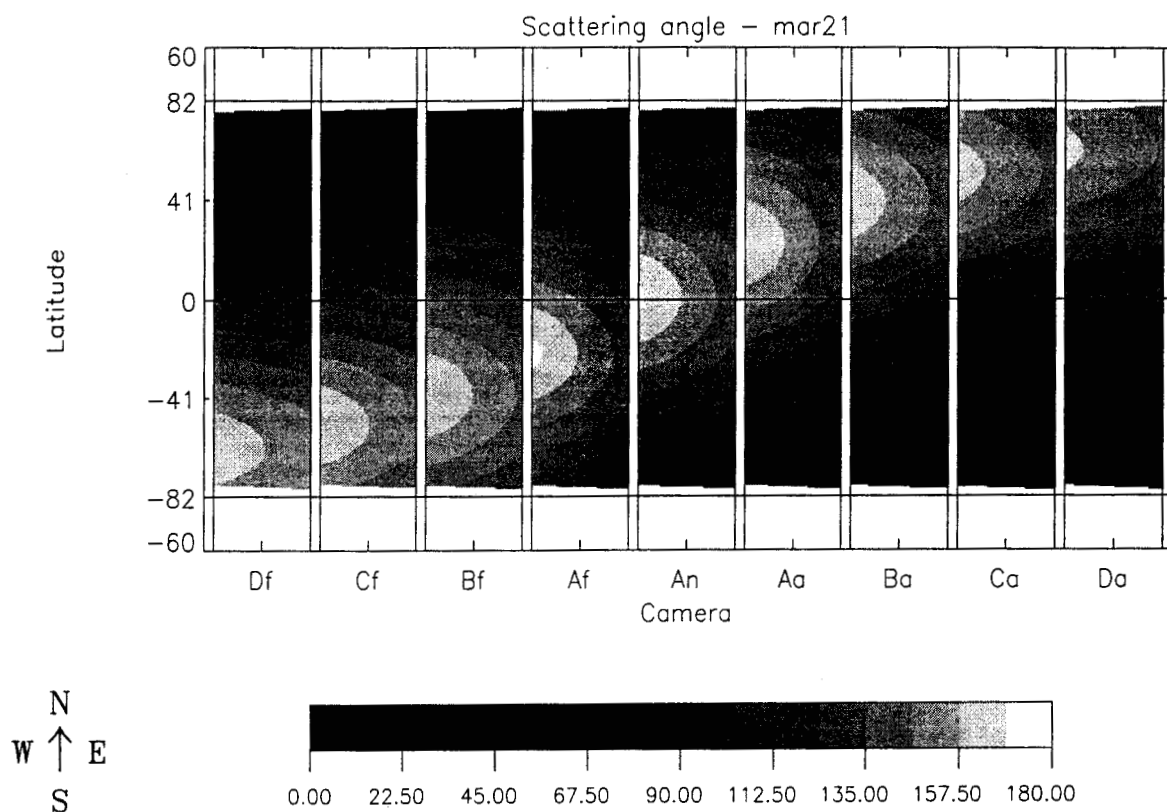


**Figure 3. Scattering angles obtained across each camera's FOV on March 21**

The areas at the top and bottom of Figure 3 are reserved for data acquired on the ascending portion of the orbit on dates other than the equinoxes. On March 21, coverage is approximately symmetrical between the northern and southern hemispheres and observations extend to about  $\pm 80^\circ$  latitude. Scattering angle coverage  $> 150^\circ$  is obtained at all latitudes. Due to the relatively flat phase function between about  $120^\circ$  and  $150^\circ$  and absence of a glory in the backscattering from irregularly shaped particles, MISR observations are expected to provide an observational means of distinguishing between spherical and non-spherical particles with characteristics typical of natural aerosols [61].

## 6. SURFACE RETRIEVALS

### 6.1 OBJECTIVES

About 30% of the Earth's surface is covered by land and much of this is vegetated. Surface processes are important components of the terrestrial climate system [20]. In particular, continents affect the climate system because of

- (1) Their orography, which substantially modifies the planetary atmospheric flow;
- (2) Their relatively small heat capacity, compared with that of the oceans, which induces a range of dynamic perturbations, from sea-breezes to monsoons;
- (3) The very high spatial and temporal variability of terrestrial surfaces, which affect the roughness of these surfaces, and therefore the dissipation of atmospheric kinetic energy through friction and turbulence;
- (4) Their albedo and, to a lesser extent, emissivity, which are highly variable in space and time, and which control the absorption of solar and the emission of thermal radiation, respectively, hence the bulk of the energy available in the climate system;
- (5) Their hosting of most of the biosphere (over 99% by mass), which exerts significant controls on the exchange of heat, moisture, and chemicals within the climate system, through a surface of contact (that of plant leaves) which exceeds the total area of the planet's surface.

The bulk of the solar energy provided to the troposphere is first absorbed at the lower boundary (oceans and continents) and then made available to the atmosphere through the fluxes of sensible and latent heat, as well as in the form of thermal radiation. Accurate descriptions of the interactions between the surface and the atmosphere require reliable quantitative information on the fluxes of energy (all forms), mass (including water and CO<sub>2</sub>), and momentum, especially over terrestrial areas, where they are closely associated with the rates of evapotranspiration and photosynthesis. Many of these processes and interactions directly affect the reflectance of the surface [68], [108], [109]. Reflectance measurements, which can be acquired by remote sensing, are therefore particularly useful to describe and predict these surface-atmosphere interactions. Clearly, the usefulness of such measurements is not limited to vegetated areas, as all significant modifications of surface properties, whether due to natural or human-induced causes, tend to affect this property. While these changes may impact on the state of the climate system through a perturbation of the boundary condition at the bottom of the atmosphere [9], [21], [84], they also provide a unique opportunity for their detection through remote sensing techniques.

Angular signature information is also expected to be a significant component of improved surface cover classification and characterization. The time-evolution of terrestrial ecosystems is difficult to monitor at the surface and satellite platforms provide a unique opportunity to carry out extensive surveys with comprehensive spatial coverage and high time resolution. Detection of eco-

physiological change on the land surface, resulting from natural processes (canopy succession and species replacement) or anthropogenic activities (e.g., deforestation, acid rain), necessitates accurate, repeatable measurements of the surface that can be used for landscape classification. Consequently, a major measurement objective of the MISR investigation is to characterize the bidirectional reflectance distribution function of all terrestrial surfaces, as a function of space, time, and surface type. Over oceans, monitoring of ocean color provides the means of monitoring marine biological productivity and its changes with time.

The overall scientific objectives of the MISR surface retrievals are:

- (1) To study, on a global basis, the magnitude and natural variability in space and time of sunlight absorption and scattering by the Earth's surface, particularly through determination of the surface hemispherical reflectance (spectral albedo);
- (2) To provide improved measures of land surface classification and dynamics in conjunction with MODIS;
- (3) To supplement MODIS observations of ocean color in the tropics by providing atmospherically-corrected water leaving radiances in the equatorial regions.

Further background on each of these objectives is presented below.

### **6.1.1 Surface radiative fluxes**

It is well known that natural surfaces do not behave as lambertian scatterers but exhibit anisotropic reflectance properties which depend on the characteristics of the surface. In general, the reflected radiance from a given surface type is a function of the solar zenith angle, the viewing zenith angle and the difference between the solar and viewing azimuth angles. Surface retrievals require removing the effects of the atmosphere from MISR multi-angle measurements (termed an atmospheric correction). Determination of the atmospheric model to be used as input to the atmospheric correction is described in [M-10]. Integration of the retrieved directional reflectances over the whole hemisphere of viewing angles defines the hemispherical reflectance (spectral albedo) of the surface. Using solely nadir spectral reflectance factors, surface hemispherical reflectance cannot be estimated with an accuracy of better than about 45%; over vegetated terrain, for example, the accuracy cannot be improved to better than about 25% even when physical models of the canopy are invoked [68]. Kimes et al. [68] showed that integration over the upward hemisphere of multi-angle measurements obtained in azimuthal "strings", that is, at multiple view angles in a plane of approximately constant azimuth angle with respect to the solar incidence direction, will provide estimates of surface radiative fluxes over vegetated and non-vegetated terrain with significantly improved accuracies.

### 6.1.2 Land surface classification

Hall et al. [49] showed how time series of satellite data could be used to monitor ecosystem dynamics over large areas, a task that was infeasible prior to the advent of satellite remote sensing. Such monitoring is important to (1) determine the level of direct anthropogenic impact on the land biota and (2) detect species compositional “drift” in response to environmental perturbations, whatever their origin. Although spectral data provide some information on the physiological state of vegetation, inference of the structural properties of the three-dimensional vegetation stand is also required, and it is difficult to determine canopy architecture and states (e.g., biomass, leaf area index) from a single view angle [33], [67]. Measurements of directionally reflected radiation can be analyzed by means of physical surface models which provide information about the physical and optical properties of the surface [94], [130]. To the extent that coupled, physically-based surface-atmosphere models can be successfully inverted against satellite remote sensing data, the retrieved values of the model variables may be useful for the purpose of land surface classification.

The MODIS instrument on the EOS-AM platform, because of its near-synoptic global coverage, will provide key observations for studies of ecosystem dynamics, the spatial distribution of vegetation community composition and species (CCS) and the time rate of change in CCS. However, this high-temporal resolution coverage is obtained at the price of combining data obtained over a wide field-of-view, and consequently obtained at a multitude of observing angles. In this case, the non-lambertian character of the surface reflection can be regarded not as the signal, but as a source of error. Therefore, characterization of the multi-directional reflectance properties of various types of surface cover with MISR will enable the development of angular reflectance models that will enable the correction of MODIS observations for the effects of wide-angle viewing.

### 6.1.3 Ocean surface observations

Marine phytoplankton are the basic link in the ocean food chain and are responsible for roughly the same amount of photosynthesis as is performed by land vegetation. The concentration of chlorophyll *a* and its degradation products (known as phaeopigments) have been used to estimate the rate of biological productivity in ocean waters. The primary instrument for assessing ocean productivity on EOS-AM is MODIS. When the satellite passes over the solar equator, some imagery is lost due to sun glint. Because MISR acquires images continuously at several angles, atmospherically-corrected water-leaving equivalent reflectances (see below), uncontaminated by sun glitter, will be obtained in this region. With the MISR spectral band set, chlorophyll pigment concentration is estimated by forming the ratio of the equivalent reflectances in the blue (443 nm) and green (555 nm) bands [40]. Since MISR does not include bands between 443 nm and 555 nm, only the low phytoplankton pigment concentration range (0 - 1 mg pigment/m<sup>3</sup>) will be available; however, this should be sufficient for most of the tropical oceans.

## 6.2 HISTORICAL PERSPECTIVE

The MISR surface retrievals will generate a number of parameters related to the surface science objectives outlined above. Over land, these include hemispherical-directional reflectance factor (HDRF), bidirectional reflectance factor (BRF), bihemispherical reflectance (BHR), directional-hemispherical reflectance (DHR), a parametric model of the surface BRF, and the fraction of incident photosynthetically active radiation absorbed by live vegetation (FPAR). Over ocean, these include equivalent reflectance and phytoplankton pigment concentration. A summary table defining these and related surface-atmosphere radiation interaction terms is provided in Table 4. This section provides a brief historical perspective on the determination of the surface retrieval parameters, and how MISR's retrieval approach fits into the current state-of-the-art.

**Table 4: Surface parameters and related surface-atmosphere radiation interaction terms**

Term	Name	Definition	Units
BRDF	Bidirectional Reflectance Distribution Function	Surface-leaving radiance divided by incident irradiance from a single direction	$\text{sr}^{-1}$
BRF	Bidirectional Reflectance Factor	Surface-leaving radiance divided by radiance from a lambertian reflector illuminated from a single direction	--
HDRF	Hemispherical-Directional Reflectance Factor	Surface-leaving radiance divided by radiance from a lambertian reflector illuminated under the same ambient conditions	--
DHR	Directional Hemispherical Reflectance	Radiant exitance divided by irradiance under illumination from a single direction	--
BHR	Bihemispherical Reflectance	Radiant exitance divided by irradiance under ambient illumination conditions	--
FPAR	Fractional absorbed Photosynthetically Active Radiation	PAR irradiance absorbed by live vegetation divided by incident PAR irradiance	--
$\rho$	Equivalent reflectance	$\pi \cdot$ radiance divided by normal incidence irradiance	--
C	Phytoplankton pigment concentration	Concentration of chlorophyll <i>a</i> + concentration of phaeophytin <i>a</i>	$\text{mg m}^{-3}$
L	Spectral radiance	Radiant energy per time-area-solid angle-wavelength interval	$\text{W m}^{-2} \text{sr}^{-1} \mu\text{m}^{-1}$
E	Spectral irradiance	Incident radiant energy flux	$\text{W m}^{-2} \mu\text{m}^{-1}$
M	Spectral radiant exitance	Surface-leaving radiant energy flux	$\text{W m}^{-2} \mu\text{m}^{-1}$

### 6.2.1 Land surface HDRF and BRF

The majority of effort in retrieving surface reflectance factors involves accurate correction for the effects of atmospheric scattering and absorption. It is well established that atmospheric effects are responsible for dramatic modifications of the spectral and radiometric content of remotely sensed images of the Earth's surface. Generally, the problem consists of two parts: (1) finding the state of the atmosphere at the time the surface observations were acquired, and (2) inverting the top-of-atmosphere radiances to obtain surface reflectance properties. The first problem is dealt with in [M-10]. The second problem is dealt with in [M-11]. The atmospheric correction problem is particularly significant for MISR because the off-nadir observations accentuate the effects of the atmosphere.

There is a considerable body of literature devoted to the atmospheric correction problem for remotely-sensed land surface images, particularly with application to Landsat. Extensive reference lists may be found in [64] and [116]. Because Landsat is nadir-viewing, most of the literature deals with this case, although there has been increased attention to the problem of off-nadir viewing and atmospheric effects and their correction in the presence of non-lambertian surfaces [24], [25], [72], [115], [121].

Most current surface retrieval (i.e., atmospheric correction) methodologies describe the top-of-atmosphere signal in terms of radiative transfer theory for a scattering (and partially absorbing) atmosphere above a spatially-variable non-lambertian surface boundary. This approach is adopted for MISR. Rapid inversion of the radiative transfer equation is necessary in order to implement an operational surface retrieval. Speeding up the retrievals usually involves one or more approximations to deal with multiple scattering in an efficient way (e.g., Liang and Strahler [75] use a four-stream approach for the multiply-scattered field). The approach adopted for MISR deals with multiple scattering within the atmosphere exactly (that is, to within numerical uncertainties). The improvements in efficiency are found by dealing with multiple bounces between the surface and atmosphere in an approximate way [M-11]. The algorithm results in retrieval of surface HDRF as well as surface BRF. The HDRF, because it is defined for the actual illumination conditions, including diffuse skylight as well as direct sunlight, is useful for climate modeling and for comparison with field measurements. The BRF, on the other hand, is defined for illumination by direct sunlight only, and thus is more useful for the purpose of determining the physical state of the surface from angular shape information. Retrieval of BRF requires assumption of a model describing the bidirectional reflectance properties of the surface, because it is necessary to correct for the diffuse skylight illumination. We use an empirically-derived, parametric formulation to carry this out [M-11].

### 6.2.2 Land surface BHR and DHR

To determine surface hemispherical reflectance of localized regions (i.e., on spatial scales of

a few kilometers), narrow field-of-view sensors, which provide (1) high spatial resolution, (2) multi-angle observations within a short period of time, and (3) nearly invariant spatial footprints as a function of view angle, are required. Given these conditions, radiances from the same scene, measured more or less coincidentally at several different angles, can be directly integrated to yield the hemispherical flux. Earlier satellites, notably Nimbus-7 (ERB) and NOAA-9 (ERBS), have pioneered the beginnings of this technique, though at resolutions much coarser than generally of interest to the land surface community. The Nimbus-7 scanner reduced its FOV to keep the viewed area about the same size, but had to look at different scenes across track and build up directional models in a statistical sense [122]. In its along-track mode the NOAA-9 scanner obtained a very limited data set looking at fixed regions, but since its scanner had a fixed FOV the size of the target area changed systematically with angle. At the footprint size to be used for MISR surface parameters, the size of the target area will be approximately constant with angle, thus enabling a separation of angular reflectance effects from the effects of changing target area.

### 6.2.3 Parametric models of bidirectional reflectance factor (BRF)

The use of a parametric model for the angular distribution of reflected light from terrestrial surfaces as a function of view and illumination geometry serves two distinct purposes:

- (1) A BRF model enables a full characterization of the reflectance properties of the surface by the prediction of the amount of light reflected in all directions, besides those observed by the sensor, and extension of hemispherical reflectance to solar illumination geometries not encountered in the sun-synchronous orbit;
- (2) If a correspondence between the values of the parameters and the physical characteristics of surface scenes can be established, the BRF parameters can be used as scene classifiers.

The oldest parametric models can be found in the planetology literature (e.g., [83]). These types of models have been used over clouds and terrestrial surfaces (e.g., [35]), and later extended to account for azimuthal variations, hot spot effects, and specularities [1], [93], [96], [98]. These models are generally non-linear functions of the parameters. Another approach has been proposed, under the form of “linearized models”, based on the assumption that the reflectance of a complex surface can be described as the sum of two or more terms, for instance a volume and a surface contributions [105], [131].

To meet the first objective described above, the models are not required to be physically based. However, for the purpose of characterizing the physical and optical properties of the surface, physically-based models have an advantage for retrieving accurate and reliable values of the state variables of the system from a quantitative analysis of the measurements (e.g., [36]). Others, including [60], [51], and [79] pioneered the extension of the classical radiative transfer theory to account for compact media in planetology. Ross [101] pursued similar objectives in the case of terrestrial vegetation, and provided a broad physical and mathematical background to discuss the



architectural and leaf orientation effects of plant canopies. The application of standard radiation transfer theory to vegetation layers was investigated in depth by Shultis and Myneni [114]. They included the formulation of the extinction and scattering coefficients of Ross in the original radiative transfer equation to account for the anisotropic scattering properties of leaves. Further studies introduced physically-based models to represent the hot spot effect explicitly as a modification of the effective optical depth in complex media composed of oriented, finite size scatterers [89], [130], while others investigated the effect of the hot spot on the first order of scattering [57], [70], [80]. Developments have also taken place to account for the physical coupling between the vegetation, the underlying soil, and atmospheric layers, through the specification of appropriate boundary conditions [32], [75], [88].

Recent model developments have thus tended towards increasing levels of complexity. At the present time, methods of representing the full three-dimensional heterogeneity of the scenes of interest and of solving the corresponding three-dimensional radiation transfer equation are being pursued [86]. This difficult question had already received a partial solution through the work of Otterman [90] and Li and Strahler [73], [74] who proposed to describe the canopy as an assemblage of geometrical opaque or semi-transparent objects casting shadows. Other three-dimensional approaches include radiosity-based methods [5], computer graphics techniques [37], and Monte-Carlo or ray tracing techniques [43], [66], [102]. These approaches require a minimum number of assumptions to represent the transfer of radiation, and can model detailed and complex scenes; however, they are quite computationally intensive.

The selection of a particular model to represent the surface bidirectional reflectance involves a trade-off between the nature and number of state variables on the one hand, and the number of hypotheses or computational cost that can be afforded on the other. Because retrieval of the surface bidirectional reflectance distribution using MISR data must be computationally efficient, complex radiative-transfer based calculations are not viable during routine processing. Thus, we adopt the approach of using a simple parametric form which can be linearized via simple transformations to characterize the BRF. This is necessary for the purposes of objective (1) above, as there is a need to perform real-time retrievals of the model parameters which can be extremely inefficient if the model cannot be transformed into a linear form. However, as we are also interested in objective (2), that is, interpreting the retrieved parameters in terms of physical properties of the surface, such as leaf area index or leaf angle distribution, a correspondence must be established between the numerical values of the parametric model and the characteristics of a physically-based model. Identifying such a correspondence will provide the means of mapping the BRF parameters into the surface physical properties and classifying the scene. As an extensive, global multi-angle and multi-spectral data set is acquired by MISR and MODIS following launch of EOS-AM, we can expect that further developments in the use of such data in retrieval or inversion schemes to characterize the physical properties of the surface will be stimulated, and new ideas will be tested.

#### 6.2.4 Fractional absorbed photosynthetically active radiation (FPAR)

The productivity of vegetation is related, among other factors, to the amount of incident photosynthetically active radiation (400 - 700 nm) absorbed by the photosynthesizing tissue in a canopy, parameterized by the ratio of absorbed to incident radiation, FPAR. An accurate specification of FPAR is a crucial factor in the estimation of large-scale productivity and carbon budget models [95], [97], [106]. FPAR or its surrogate can be vicariously determined from remote observations of surface spectral reflectance on the premise that surface structural and optical properties govern radiation absorption and scattering in a canopy [125]. There is substantial empirical evidence to suggest that FPAR is related to top-of-the-canopy spectral vegetation indices ([2], [16], [31], [50], [135] among others). This has also been demonstrated quasi-theoretically using radiative transfer models of varying degree of detail ([3], [4], [10], [44], [87], [108] among others).

While this body of evidence is impressive, there has been only one effort at extracting FPAR from satellite data [78], [110]. It is a  $1^\circ \times 1^\circ$  monthly data set produced from nine years (1982-1990) of AVHRR GAC data, with Fourier interpolation, data reconstruction and sun-angle corrections. The algorithm is described in detail in [78] and [110]; it suffices here to note that the algorithm is not based on physical principles of remote sensing but on heuristic corrective methods to obtain spatially continuous multi-year data sets of surface variables. Current efforts at producing improved FPAR and other surface variable data sets are hampered largely by a lack of atmosphere-corrected multi-spectral and multi-angle surface reflectance observations, such as those envisioned in the EOS era. Additional improvements in the determination of FPAR that may be expected from MISR include the potential of classifying the surface from angular signature information, in order to establish the optimal relation between FPAR and vegetation index, and using PAR-integrated BHR in more direct approaches to deriving plant productivity and FPAR.

#### 6.2.5 Ocean surface equivalent reflectances

Correction for atmospheric scattering over oceans is essential for studies of ocean color because the low reflectance of the ocean surface (away from sun glitter) result in the signal being dominated by Rayleigh and aerosol backscatter. Gordon et al. [40] have developed operational atmospheric correction algorithms for use with Coastal Zone Color Scanner (CZCS) imagery. These algorithms are based on observations in the red and near-IR, where ocean water is nearly black, and the weak dependence of typical marine aerosol scattering phase function with wavelength means that the radiance backscattered out of the ocean can be estimated with sufficient accuracy at  $\lambda > 500$  nm to determine the relative spectral variation of the aerosol optical depth [39]. This, in turn, provides a good estimate of the gross features of the aerosol size distribution [41], although a scattering model (e.g., Mie theory) and an estimate of the refractive index of the aerosol were needed to calculate the absolute values of the aerosol phase function and optical depth. With the wider spectral coverage of SeaWiFs and MODIS, the CZCS algorithm can be improved [42]. The multi-angle coverage of MISR enables further refinement of the aerosol model [M-10].

### 6.3 BENEFITS OF MULTI-ANGLE VIEWING

The multi-angle viewing strategy of MISR provides information about the surface in several ways:

- (1) It enables retrieval of atmospherically corrected directional surface reflectances that can be integrated to obtain more accurate estimates of hemispherical albedo than can be obtained with single-view-angle observations;
- (2) The multi-angle data will enable both the inversion of physical angular reflectance models and establishment of off-nadir corrections for MODIS;
- (3) The nine cameras provide coverage in scattering angle,  $\Omega$ , which is the angle between the direction of the Sun's rays and the direction to the sensor (see Figure 3).

With regard to the last point, two regimes are of primary interest: scattering angles near  $180^\circ$ , where reflection from certain surface covers, such as vegetation canopies, show a brightness enhancement, or "hot spot" (e.g., [34]), due to the absence of shadows, and forward scattering angles close to the specular reflectance direction, where sun glitter effects are observed. With regard to the first point, Figure 4 shows the view azimuth angle (the difference between the view and solar incidence planes in a local surface coordinate system) as a function of field angle in the nine MISR cameras and as a function of latitude.

Systematic studies of the accuracies of hemispherical reflectance estimates from multi-angle images have been undertaken [68]. These studies demonstrated that the most accurate estimates are obtained when the data are acquired in at least two azimuthal strings, where a "string" is a sequence of observations with variable view angle in a more-or-less constant azimuthal plane relative to the solar incidence direction. For two strings, best results are obtained when they are significantly separated in azimuth. In addition, the highest accuracy is obtained when the strings are close to the  $45^\circ$  and  $135^\circ$  planes. A theoretical argument supporting this empirical observation is presented in [68].

Figure 5 shows predicted equivalent reflectances across the MISR camera FOV's over an ocean surface with a wind speed of 5 m/sec, calculated according to the Cox and Munk [14] model. Note the glint region near the equator in the nadir camera. MODIS data will be similarly affected. Observations in the same region, but with the B cameras, significantly reduce the glitter.

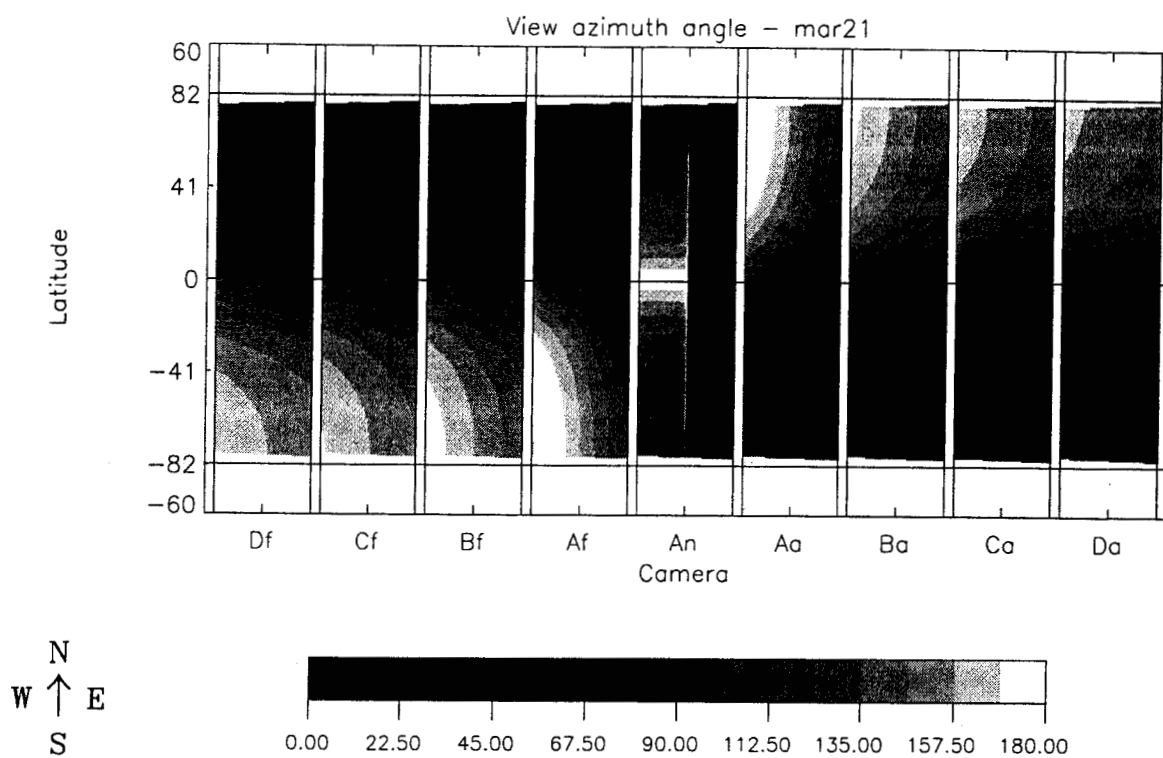


**Figure 4. View azimuth angles obtained across each camera's FOV on March 21**

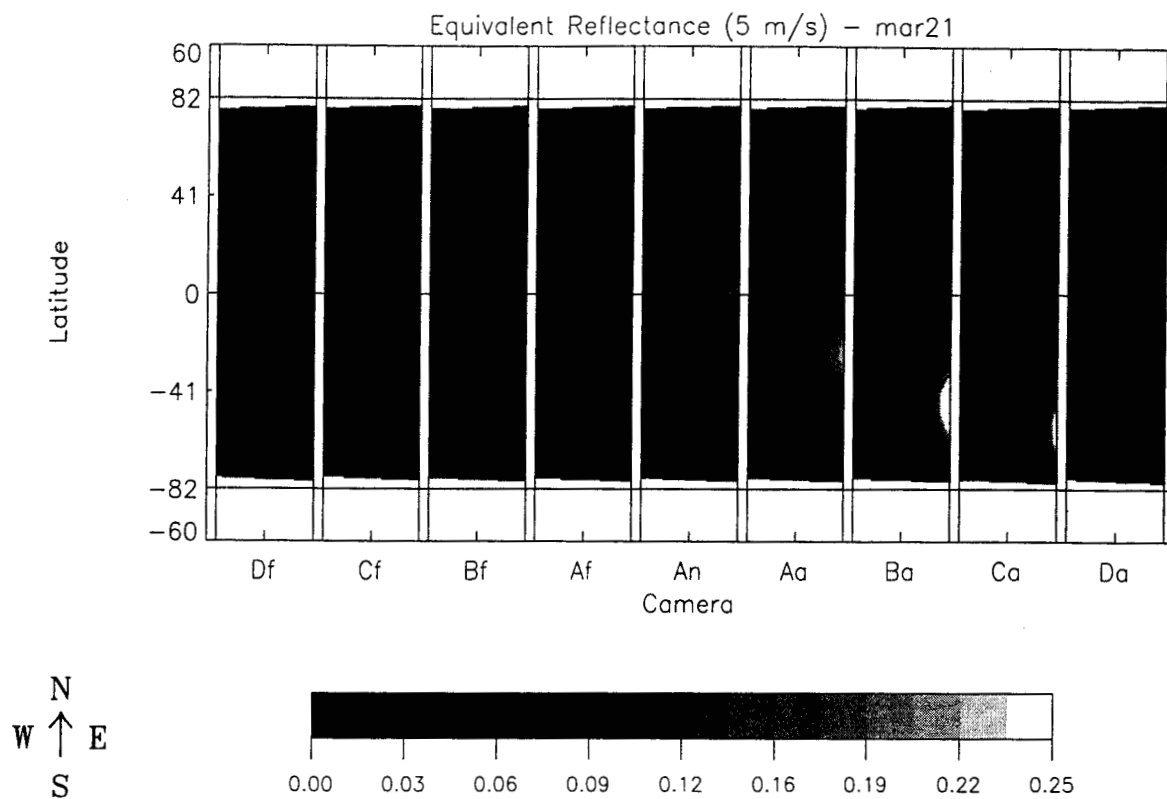


**Figure 5. Ocean sun glint patterns obtained on March 21 for surface wind speed = 5 m/sec**

## 7. CLOUD STUDIES

### 7.1 OBJECTIVES

As a result of their large areal extent, high albedo, and variability on many length and time scales, clouds play a major role in governing the Earth's energy balance. Regional studies of the impact of clouds on the energy balance require measurements of the radiation budgets as a function of scene type. The importance of cloud characteristics in global studies of climate has been well documented [107]. Current theories and models of the response of the Earth's climate system to, for example, the increase in trace gases, are severely limited by our present ignorance of the feedback processes associated with changes in cloud amount and cloud properties. In this respect, two issues are paramount. One is the realistic modeling of cloud-radiation interaction taking into account the variable structure of broken cloud fields and processes that occur at the sub-grid scale level of present general circulation models. The other is the ability to invert satellite measured radiances to obtain hemispherical fluxes with sufficient resolution to discriminate between cloud-filled and cloud-free scenes.

Deriving from its ability to measure any scene from multiple directions, MISR will contribute unique information about top-of-the-atmosphere shortwave radiation. The most important elements of the MISR retrievals are accurate spectral albedos and spectral bidirectional reflectance factors, coupled to useful scene information, such as parameterizations of the cloud morphology.

The overall scientific objectives of the MISR top-of-atmosphere and cloud investigations are:

- (1) To detect clouds as a prerequisite to scene classification and to identify cloud-free lines of sight prior to the application of aerosol and surface retrieval algorithms;
- (2) To classify different types of cloud fields by their heterogeneity and altitude;
- (3) To study, on a global basis, the effects of clouds on the spectral solar radiance and irradiance reflected to space, including spatial and temporal dependences.

Further background on these objectives is presented below.

#### 7.1.1 Cloud detection and screening

Cloud detection is used to (1) determine whether a scene is classified as clear or cloudy for the purpose of choosing the angular integration coefficients which are used in estimating TOA albedos, (2) calculate regional cloud cover, and (3) determine whether a scene is clear enough to perform aerosol and surface retrievals.

Applying traditional cloud screening methods to each MISR camera is a challenging prob-

lem given the small number of spectral channels available, none of which are longward of  $1\ \mu\text{m}$ . As a result, only a few simple cloud detection observables can be constructed from arithmetic operations on the camera radiances. This requires good estimates of the thresholds that will discriminate clear skies from cloudy skies. However, MISR affords the opportunity to apply multi-angle methods as well. Thus, the cloud detection approach will also be based on stereophotogrammetric methods, and on angular signature. The result of these techniques will be a Radiometric Camera-by-camera Cloud Mask (RCCM), a Stereoscopically Derived Cloud Mask (SDCM), and an Angular Signature Cloud Mask (ASCM). The RCCM makes use of bidirectional reflectance factors, at each angle independently, in the MISR red and near-IR bands. Different observables are used over land and water. The SDCM is derived as part of the stereoscopic retrieval of the Reflecting Level Reference Altitude (RLRA), described below. The ASCM is geared toward the detection of cirrus, and takes advantage of the difference in the Rayleigh signal above high clouds between blue and red or near-IR wavelengths as a function of angle. High clouds have a unique signature that distinguishes them from clear sky and low-level clouds. The ASCM is based on a method known as Band-Differenced Angular Signature [22], [23].

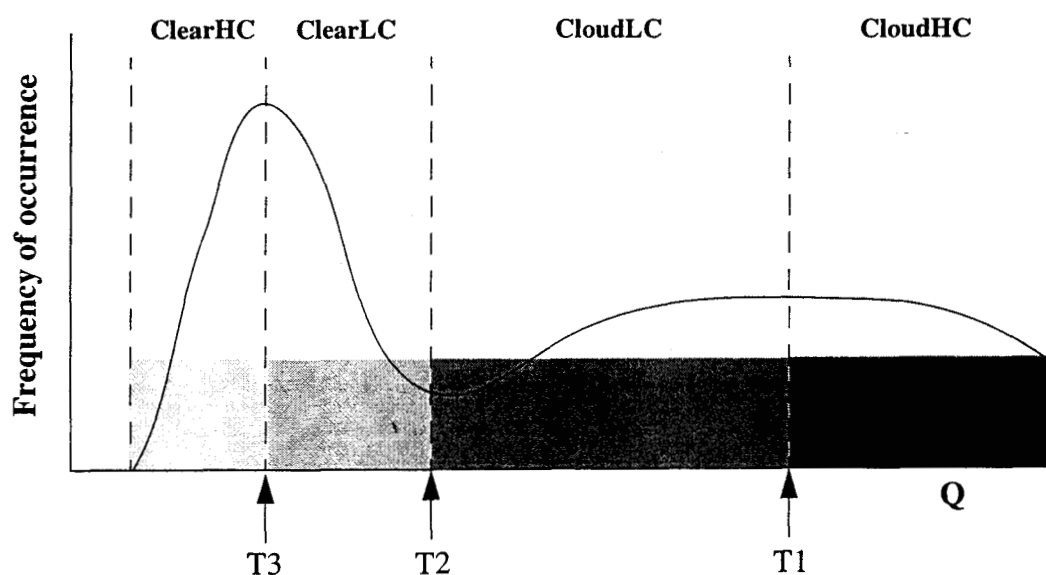


**Figure 6. Schematic view of cloud thresholding on an observable,  $Q$**

In the case of the RCCM and ASCM, each observable will be tested by comparing to three thresholds in order to classify the pixel as cloud with high confidence (CloudHC), cloud with low confidence (CloudLC), clear with low confidence (ClearLC), or clear with high confidence (ClearHC). The Support of Environmental Requirements for Cloud Analysis algorithm is a recent example that applies confidence levels to cloud masks. The thresholds are derived from time cumulated statistics, for a particular observable, and for a particular region. Figure 6 shows a hypothetical example of a one-dimensional distribution of an observable,  $Q$ . The RCCM observables for water tend to have a

clear conditions, whereas the land observables tend to have a peak at low values representing cloud. The thresholds are a function of view angle, sun angle, relative view-sun azimuth angle, time, and surface classification. The time dependence can be of three kinds: (1) time independent (static), (2) dynamic (seasonal), and (3) dynamic on a monthly time scale. They are derived from the histograms using an automated procedure.

In the case of the SDCM, the thresholds are static, and are referenced to the surface elevation. The confidence levels in the SDCM are derived as part of the stereoscopic processing that is performed in generating the RLRA.

### **7.1.2 Cloud classification**

Accurate cloud height is recognized as one of the principal characteristics which is lacking in existing cloud climatologies [107] as well as being poorly represented in existing studies of severe storm phenomena [91]. The difficulty in obtaining reliable estimates of cloud-top altitude continues to hamper many efforts to model the three-dimensional field of radiative fluxes which play a critical role in climate feedback.

Multi-angle imagery from MISR creates opportunities to reconsider some conventional approaches to remote sensing. The stereo retrieval of cloud heights need not be restricted to a single pair of images; multiple views obtained from satellite altitude over a wide angular range provide, for example, the ability to independently separate the effects of wind displacement from height. Three-dimensional cloud effects can be studied using statistical summaries of the scene as a function of view angle, e.g., in the form of texture measures.

In order to establish a parameter that serves the purpose of providing a classification scheme that incorporates cloud altitudes, and which also serves as a dynamic (i.e., spatially varying) reference altitude for co-registering the multi-angle views, a reference level known as the Reflecting Level Reference Altitude is established. The RLRA is defined to be the level found by matching features (or areas) with the greatest contrast in the near-nadir viewing directions. Physically, this corresponds to the main reflecting layer, which will typically be either the tops of bright clouds, or under atmospheric conditions corresponding to clear skies or thin cloud, it will be located at the surface. The RLRA is defined over areas measuring 2.2 km x 2.2 km. The algorithm for retrieving RLRA is stereophotogrammetric in nature [M-8]. For scene classification purposes, the RLRA and the associated SDCM, described above, are used to generate regional altitude-binned cloud fraction metrics. The RLRA is also used as a common reference altitude for projecting the multi-angle bidirectional reflectance factors, from which texture indices will be derived. Unique to MISR is the ability to retrieve the angular signature of texture. The correspondence between these parameterizations and physical cloud type, such as distinguishing stratiform and cumuliform clouds, will be the subject of research utilizing these parameters in the post-launch era.



### 7.1.3 Cloud climatic effects

One of the objectives of the MISR top-of-atmosphere (TOA) and cloud retrievals is to determine the spectral albedos of different cloud types. Since some clouds change substantially over short distances, it is desirable to characterize cloud type, as well as to measure the associated cloud albedo, at high resolution. Based on a study of Landsat scenes, for example, Wielicki and Parker [136] suggest that cloud retrievals can be resolution dependent over distances as short as 250 m for certain types of cloud. The intrinsic resolution of MISR is consistent with this spatial scale; however, for the at-launch product the finest resolution used for the reporting of albedo will be the scale of the RLRA, that is, 2.2 km x 2.2 km. This resolution (termed “fine” resolution to distinguish it from other albedos at “coarse” resolution, or 35.2 km x 35.2 km) is chosen as a compromise that involves considerations of archival data volume, processing time to obtain the RLRA, expected accuracy of the RLRA, and a desire to match spectral albedo to cloud properties at high resolution.

#### 7.1.3.1 Fine albedos

Calculation of spectral albedos based on multi-angle views requires the RLRA to be a dynamic (i.e., spatially varying) reference level. If the different views are simply referenced to the same static reference altitude, two sources of error would affect the albedos: disparities due to differences in height from the reference altitude, and disparities due to advection of the scene during the time between different views. To correct for these disparities we must co-register the nine different camera measurements to the same reference altitude. As described above, this altitude should be closely associated with that of the main reflecting surface, and this will generally be highly variable due to natural variability. For scenes in which the horizontal contrast in scene reflectivity is associated with a relatively unique cloud-top altitude, the RLRA corresponds directly to that altitude. For more inhomogeneous scenes, in which the contrast comes from a detectable range of altitudes, the relationship to the RLRA is more complex.

The required accuracy of the RLRA for determining spectral albedos is directly related to the horizontal inhomogeneity of the scene. Truly homogeneous scenes yield the same albedo irrespective of reference altitude, and if the D cameras, say, measure little horizontal contrast compared to the A cameras, their registration becomes of less importance. In general, the greater the horizontal contrast in measurements by a given camera, the more important it is to know what altitude is giving rise to most of the contrast so as to register that view with other views. The characteristics of sub-pixel inhomogeneities within the fine-resolution samples are measured by texture indices. These indices indicate the reliability of the fine resolution albedos (for example, lower than average levels of measured sub-sample inhomogeneity indicate higher than average accuracy in the spectral albedo); direct use of these to further improve spectral albedos for highly inhomogeneous samples is left as a research issue for the post-launch era.

### 7.1.3.2 Coarse albedos

In addition to generating fine albedos referenced to the RLRA, coarse albedos referenced to a 30-km static reference altitude is also done as part of MISR data processing. This altitude is chosen for historical reasons to enable ready comparisons with other TOA products (such as the short-wave reflected fluxes from ERBE and CERES). It also represents a reasonable altitude above which there are usually negligible shortwave effects due to scene inhomogeneities on horizontal scales of the order of 100 km. However, shortwave reflected radiation escaping through such a high reference level originates from scattering processes that are widely distributed horizontally below this altitude. For example, when the most-oblique MISR camera images are referenced to 30 km, they may measure reflection from surface features displaced about 100 km either side (along track) of the nadir view. This is an important distinction if the scene is inhomogeneous over such a scale (e.g., over partly cloudy scenes or clear land). This must be taken into account in deriving the coarse albedos.

Two coarse resolution albedos, defined over regions measuring 35.2 km x 35.2 km and referenced to 30-km altitude, are defined for MISR. For comparative purposes, especially with earlier products such as from ERBE, we define the “restrictive” TOA albedo to be the one obtained using angular integration of the observed BRF’s over the given region only, and the “expansive” TOA albedo to be the one obtained using integration over all relevant surrounding regions, that is, all regions influencing the radiative flux leaving the top of the atmosphere. Both are attributed to the same region at the TOA but they may have considerably different values.

As examples, consider first a scene that is horizontally homogeneous over  $\sim 10^3$  km in all directions. Here there is no sampling problem and the restrictive and expansive albedos should be the same. Now consider a 35.2 km wide strip of clear ocean below the TOA region in the along-track direction with continuous cloud cover on either side of this strip. The measured radiances passing through the TOA coarse region will be consistently low and will indicate a low albedo regardless of the angular integration scheme used. Yet a pyranometer at 30 km would measure a much higher shortwave flux averaged over the same area due to the cloud contributions. These differences tend to cancel when averaged over a large number of scenes, and are not relevant for homogeneous scenes. For inhomogeneous scenes, however, the expansive and restrictive albedos may differ significantly. Since these scenes have special importance to the determination of TOA shortwave cloud forcing by different cloud types, we report the results of both methods of calculation.

### 7.1.3.3 Angular integrations

To calculate albedos with MISR, the more general problem of applying a bidirectional model (chosen from some measure of scene identification, and commonly referred to as an Angular Distribution Model, or ADM) to extrapolate a *single* radiance over all zenith and azimuthal directions

in the hemisphere, is replaced by the easier problem of choosing an Azimuthal Model (referred to as an AZM) based in part on the zenith angle dependence of the observed radiances (and in part on other, less critical, information regarding the scene type) to extrapolate *nine* radiances over the hemisphere. The AZM's are used to integrate BRF's over angle to derive spectral albedos. For a particular target, the radiances measured by the nine MISR cameras lie more-or-less in a single vertical plane. Therefore the zenith angle dependence of the radiation reflected in that plane will be fairly well known. However, the reflected radiance also varies with azimuth angle. For example, most natural surfaces reflect more radiation to the solar plane than to the plane perpendicular to it. These azimuthal variations generally have a few percent effect on the calculated albedo values. Thus, models are required to facilitate the azimuthal integrations. From these models are derived sets of coefficients, categorized by scene type, that constitute predetermined look-up tables contained within a database called the AZM Dataset. The AZM coefficients depend on solar zenith angle and cloud and surface types. During routine processing, selection of the appropriate AZM coefficients depends on whether a scene has been classified as clear or cloudy by the cloud detection process.

## **7.2 HISTORICAL PERSPECTIVE**

### **7.2.1 Cloud detection and screening**

Cloud detection and screening involves discriminating between clear and cloudy pixels in an image. Reviews of cloud detection methods can be found in [38], [103], [104]. Methods for identifying clouds are generally based on radiance threshold, radiative transfer model, or statistical techniques making use of spectral and textural features in the imagery. Radiance threshold techniques work on a pixel-by-pixel basis, and single or multiple-channel thresholds are defined which are then used to divide clear and cloudy pixels. Radiative transfer model techniques use one or more spectral radiance measurements as input to an atmospheric radiative transfer model and retrieve a physical quantity such as cloud optical thickness or altitude. The pixels are then determined to be clear or cloudy based on thresholds in the retrieved quantity. Statistical techniques use groups of adjacent pixels. Among these are methods based on spatial coherency between adjacent pixels [11], neural networks (e.g., [124]), maximum likelihood decision rules (e.g., [27]), and clustering routines (e.g., [30]). Specific cloud detection algorithms applied to satellite data generally have features which are beneficial for a particular scene class.

### **7.2.2 Cloud classification**

Cloud classification by MISR should help to partition clouds into categories distinguished by parameters such as: (1) cloud elevation, (2) angular signature, and (3) texture or degree-of-brokenness (e.g., stratiform vs. cumuliform).

### 7.2.2.1 Classification by elevation

The conventional methodology for the retrieval of cloud-top elevation is to use thermal-infrared brightness temperatures which sense to the level of optical depth unity in the clouds and then to transform these brightness temperatures to an altitude based on an assumed cloud emissivity and an atmospheric temperature profile.

Stereoscopic observations from satellite provide an independent, and wholly geometric means to obtain this information without assumptions about the relationship between cloud-top radiative temperature and cloud-top pressure or dependence on ancillary information such as radiosonde data at some distance and time away from the cloud observation. Cloud analysis using stereography has a long history [53]. Apart from study of clouds and cloud regimes from both the air and ground using stereo data, Kassander and Simms [62] employed two aerial cameras at separate stations on the ground to determine cloud ranges and cloud heights. Roach [100] analyzed summit areas of severe storms using stereo photos taken from a U-2 aircraft. Whitehead et al. [134] and Shenk et al. [112] analyzed stereo photographs taken during the Apollo 6 mission to measure heights of cloud bases and tops and to study the three-dimensional structure of convective clouds. Hasler [53] made stereographic determinations of cloud heights from simultaneous scans on the GOES East and GOES West satellites by computer remapping of digital image pairs. Elevations determined in this fashion were validated using high altitude lakes; the absolute height accuracy was  $\pm 0.5$  km. Hasler et al. [54] showed that stereoscopic observations of clouds could be extracted using several different current satellite platforms, and a dedicated polar-orbiting tandem system (to eliminate cloud-motion effects) was described by Lorenz [77]. More recent experience with automated stereo matching algorithms as applied to AVHRR [85], SPOT [17] and MISR team studies with the Along-Track Scanning Radiometer (ATSR) suggest that the fore-aft viewing strategy of MISR presents the means for retrieving cloud height without the need for tandem platforms. Stereo matching to retrieve cloud elevations poses a number of challenging problems; however, the high dynamic range and signal-to-noise ratio performance of the MISR instrument and the provision of multiple views over a wide range of angles will overcome many of the difficulties encountered by more coarsely digitized sensors over low-contrast scenes.

### 7.2.2.2 Classification by angular signature

Detection of high cirrus is also important to MISR. A review of cirrus screening methods has been presented by Di Girolamo [22]. Most methods make use of at least one infrared channel. The lack of MISR channels beyond  $1.0 \mu\text{m}$  implies that the detection of optically thin cirrus on a per-camera basis will be difficult. Nadir imagers cannot always detect cirrus clouds due to restricted phase angle coverage. Therefore, the multi-angle strategy will be used in a novel way. Motivated by the future availability of MISR observations and the difficulty many current algorithms have in detecting thin cirrus, Di Girolamo [22] and Di Girolamo and Davies [23] have developed a method known as Band-Differenced Angular Signature (BDAS), a technique which takes advantage of the

difference in the Rayleigh signal above high clouds between blue and red or near-IR wavelengths as a function of angle. High clouds have a unique signature that distinguishes them from clear sky and low-level clouds [M-8].

### 7.2.2.3 Classification by texture

Cloudy scenes will be classified using textural indices sensitive to the degree of brokenness of a cloud field. Recently, textural indices have proven to be useful for cloud classification (see Gu et al. [47] for a review). For example, Welch et al. [133] used textural features alone to classify stratocumulus, cumulus and cirrus with an accuracy of 83-95% (depending on the training method). Several straightforward textural parameters, such as standard deviation divided by the mean and difference-vector standard deviation, will be included in the MISR cloud retrievals.

### 7.2.3 Cloud climatic effects

Many theoretical studies have established that plane-parallel representations of cloud fields introduce large errors in the parameterization of radiation for climate models [52], [132]. It is currently recognized that cloud modeling must consider not only the effects of individual cloud shape but also interactions such as shadowing and multiple scattering between clouds. Diffusion of radiation through the cloud sides and side illumination causes the bidirectional reflectance distribution functions (BRDF's) of cumuliform cloud fields to differ markedly from those of stratiform fields [12], [18]. However, our ability to view the same region from different angles both to characterize the scene type and to validate the theoretical model predictions has as yet been extremely limited. Coarse-resolution cross-track scanners do not see the same region from different directions, and rely heavily on scene (cloud) identification algorithms to construct statistical populations, in which data must be combined from many geographic locations to generate BRDF's. These scanners also suffer from the non-linear effects of scene heterogeneity, and can incur biases due to increasing target area with angle.

Since fluxes measured by wide-angle sensors correspond to areas  $> 10^6 \text{ km}^2$  in extent, within which the scene type is assuredly inhomogeneous, it is impossible to directly measure reflected solar hemispherical fluxes on a regional scale from satellite altitudes. Thus, to investigate the role of clouds on climate, relatively homogeneous local scenes must be observed. Then, radiances from the same scene, measured more or less coincidentally at several different angles, can be directly integrated to yield the hemispherical flux. Earlier satellites, notably Nimbus-7 (ERB) and NOAA-9 (ERBE), have pioneered this technique. The Nimbus-7 scanner reduced its FOV to keep the viewed area about the same size, but had to look at different scenes across track and build up directional models in a statistical sense [122]. In its along-track mode the NOAA-9 scanner obtained a very limited data set looking at fixed regions, but since its scanner had a fixed FOV the size of the target area changed systematically with angle. An alternative method to determine flux is to use each radiance measured by a narrow FOV instrument and invert them according to a BRDF model

relevant to the individual scene type, as was done with ERBE [117]. The presently available models have been painstakingly constructed from Nimbus-7 data, but cannot accommodate different cloud types, and define only a few categories of cloud cover amounts.

### 7.3 BENEFITS OF MULTI-ANGLE VIEWING

The multi-angle viewing strategy of MISR provides information about clouds in several ways:

- (1) The angular scattering “signature” of optically thick, heterogeneous cloud fields, along with angular contrast and texture measures, is expected to be diagnostic of their three-dimensional geometry.
- (2) The nadir and several of the off-nadir cameras will be used stereo-photogrammetrically to estimate cloud-top altitudes, for the purposes of regional scene classification and for co-registering the multi-angle views to a common reference level. Unlike single camera-pair stereo, multi-camera disparity (image translation) measurements obtained at both small and large base-to-height ratios from satellite altitudes enable compensation for the effects of motion due to wind.
- (3) The oblique viewing angles of the cameras at high off-nadir angles, particularly the C and D cameras, accentuate the signal of high thin clouds (cirrus) because of the increased optical path length through the atmosphere.
- (4) The high spatial resolution, multi-angle observations within a short period of time, and nearly invariant spatial footprints as a function of view angle, provide a novel methodology for determining the albedo of cloud fields.
- (5) The nine cameras provide coverage in scattering angle,  $\Omega$ , which is the angle between the direction of the Sun’s rays and the direction to the sensor. The single-scattering phase function of cirrus, which is dependent on scattering angle, is not well known, and MISR data will provide new information on cirrus reflective properties.

## 8. DATA PRODUCTS

### 8.1 MISR SCIENCE DATA PROCESSING

The MISR Science Computing Facility (SCF) and Distributed Active Archive Center (DAAC) represent the primary entities in which the functions of MISR science data processing will be implemented. The MISR SCF supports MISR science algorithm development, as well as quality assessment and validation of MISR data products. This will include generating those data and coefficients needed to run MISR science software at the DAAC. The MISR DAAC, which is shared with several other EOS instruments, is the facility at which software incorporating MISR science algorithms will operate in a high volume, real-time mode to produce standard science data products.

The generation of science data products can be divided into six subsystems within the Product Generation System (PGS). Each subsystem has at least one primary output product, but may have other secondary output products. It is convenient to conceptualize the processes within these subsystems as occurring in sequence, with the predecessor producing at least one complete product, a portion of which is the primary input for the successor. Each of these subsystems correspond to a processing level of a product generation flow, as shown in Figure 7. These levels conform generally to the EOS scheme from Level 1 to Level 4.

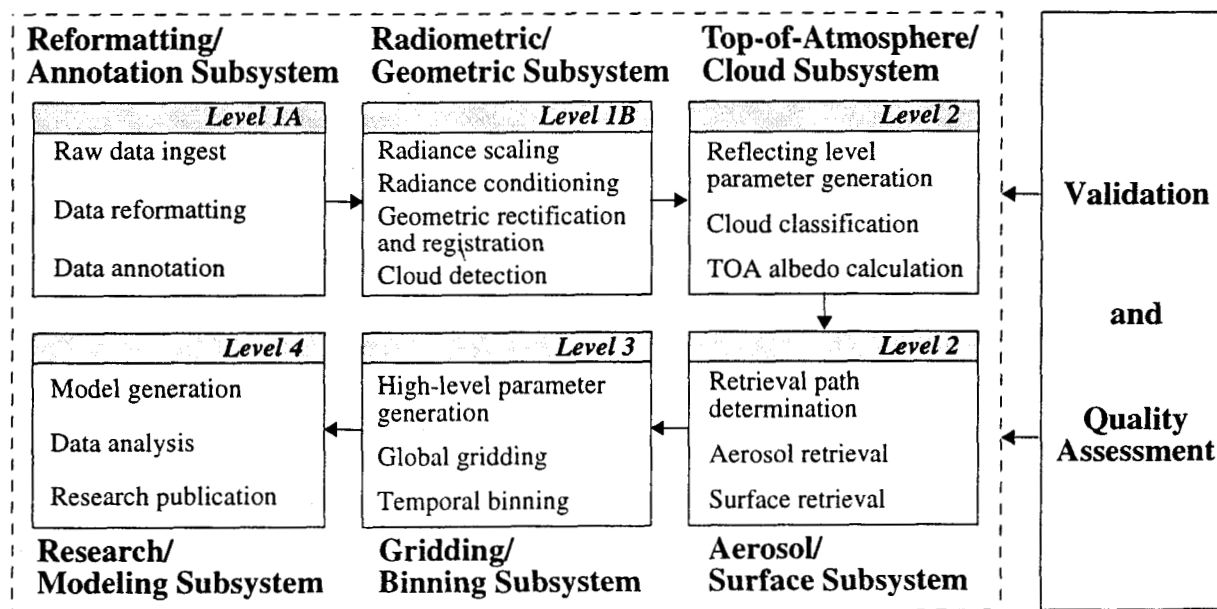


Figure 7. MISR Product Generation System

Standard products cannot be generated at the DAAC independently of the rest of the MISR science data system. They are critically dependent on calibration parameters and other lookup data, such as threshold datasets, atmospheric climatologies, aerosol and surface model datasets and the

like, which must be produced at the SCF. Functions performed at the SCF are separated from DAAC activities because they require much closer scrutiny and involvement by the MISR Science Team than the MISR DAAC could provide. Updates to these data structures occur infrequently compared to the rate of standard product generation, and therefore fit into the more limited processing capabilities of the SCF. Other essential functions that have activities at the SCF include quality assessment, algorithm and data product validation, software development, and instrument operations.

## 8.2 TERMINOLOGY

The following terms are used by the MISR project.

- (1) **Standard Product:** A product generated routinely at the DAAC.
- (2) **Ancillary Dataset:** A dataset generated at the SCF and delivered to the DAAC for use as input during routine processing. Ancillary Datasets may be updated either on a regular or sporadic basis at the SCF and new versions delivered to the DAAC, or in some cases, automated updating may occur at the DAAC. Ancillary Datasets are not required by users of MISR data to interpret the contents of Standard Products.
- (3) **Ancillary Product:** A product generated at the SCF and delivered to the DAAC for use during routine processing or as a supportive product necessary for the interpretation of Standard Products. Ancillary Products may be updated either on a regular or sporadic basis at the SCF and new versions delivered to the DAAC. Ancillary Products are distinguished from Ancillary Datasets in that they are needed by users of MISR data to interpret the contents of Standard Products.
- (4) **Parameter:** A variable contained within a product.
- (5) **External Data:** Data used during DAAC processing derived from a source other than MISR. This includes data from other instruments on the same spacecraft, other spacecraft, or non-spacecraft data such as meteorological information generated by global atmospheric models.

## 8.3 PRODUCT SUMMARY

The following table summarizes the MISR Standard (S) and Ancillary (A) Products. Contents are described in [M-1]. The reference column in the table indicates where the algorithm theoretical basis and other descriptions are to be found.



**Table 5: MISR Standard And Ancillary Products**

<b>Name</b>	<b>Contents</b>	<b>Type</b>	<b>Processing Level</b>	<b>Reference</b>
Reformatted Annotated Product (MIS01)	Depacketized, decoded instrument data	S	1A	N/A
Radiometric Product (MIS02)	Calibrated radiances	S	1B1	[M-2], [M-13], [M-14]
Georectified Radiance Product (MIS03)	Radiances projected to surface terrain and surface ellipsoid, and radiometric camera-by-camera cloud mask	S	1B2	[M-3], [M-4]; [M-13], [M-15]
TOA/Cloud Product (MIS04)	Cloud classification parameters and albedos	S	2	[M-8], [M-9], [M-13]
Aerosol/Surface Product (MIS05)	Aerosol abundances and model identifiers; surface reflectances and reflectance factors	S	2	[M-10], [M-11], [M-13]
Global Radiation Product (MIS06)	Globally mapped and temporally averaged radiation parameters	S	3	TBD
Global Cloud Product (MIS07)	Globally mapped and temporally averaged cloud classification parameters	S	3	TBD
Global Aerosol Product (MIS08)	Globally mapped and temporally averaged aerosol parameters	S	3	TBD
Global Surface Product (MIS09)	Globally mapped and temporally averaged surface parameters	S	3	TBD
Ancillary Geographic Product (MIS10)	Surface elevation parameters, land/water identifiers on Space-Oblique Mercator grid	A	1B2	[M-6], [M-13]
Ancillary Radiometric Product (MIS11)	Calibration coefficients and instrument performance parameters	A	1B1	[M-7], [M-14]
Aerosol Climatology Product (MIS12)	Optical scattering and extinction properties and physical attributes of pure aerosol particles and aerosol mixtures used in retrievals, and their climatological likelihoods	A	2	[M-12], [M-13]

## 8.4 DATASET SUMMARY

The following table summarizes the MISR Ancillary Datasets. Contents are described in [M-1]. The reference column in the table indicates where the algorithm theoretical basis and other descriptions are to be found.

**Table 6: MISR ancillary datasets**

Name	Contents	Reference
Geometric Calibration Dataset	Projection parameters, reference orbit imagery, and geometric camera model	[M-7], [M-15]
Cloud Screening Surface Classification (CSSC) Dataset	Surface types for cloud screening	[M-4], [M-13]
Radiometric Camera-by-camera Threshold Dataset	Thresholds used for generation of cloud mask during Level 1 processing	[M-4], [M-13]
Radiometric Camera-by-camera Histogram Dataset	Histograms of Level 1 cloud detection observables for dynamic updating of thresholds	[M-4], [M-13]
Angular Signature Threshold Dataset	Thresholds used for generation of cloud mask during Level 2 processing	[M-8], [M-13]
Angular Signature Histogram Dataset	Histograms of Level 2 cloud detection observables for dynamic updating of thresholds	[M-8], [M-13]
Azimuthal Model (AZM) Dataset	Angular integration coefficients for generation of top-of-atmosphere albedos	[M-9], [M-13]
Tropical Ocean Atmospheric Correction (TOAC) Dataset	Atmospheric correction data for implementation of ocean color retrieval	[M-12], [M-13]
Terrestrial Atmosphere and Surface Climatology (TASC) Dataset	Climatological values of ozone abundance, meteorological variables, and snow/ice cover to be used as defaults during processing	[M-12], [M-13]
Simulated MISR Ancillary Radiative Transfer (SMART) Dataset	Top- and bottom-of-atmosphere radiometric parameters used during aerosol and surface retrievals	[M-12], [M-13]
Ancillary Land Biome Dataset	Classification of land surface into six biomes	[M-12]

## 9. DATA PRODUCT VALIDATION AND QUALITY ASSESSMENT

### 9.1 VALIDATION

Algorithm validation consists of intercomparisons of parameters generated using MISR algorithms operating on radiance measurements from MISR aircraft simulator or spaceborne instruments with similar products generated using conventional ground-based solar and atmospheric observations, together with conventional methods of analysis and inversion. These intercomparisons may also serve in some instances to validate the assumed aerosol climatology and surface reflectance models used in the retrievals.

Validation of the aerosol and surface retrieval algorithms rely on several sources of data including aircraft observations, together with field observations of downwelling diffuse sky spectral radiance and irradiance, the direct solar irradiance component and the surface spectral bidirectional reflectance factor (BRF). In contrast to MISR spacecraft or aircraft observations of the upwelling radiation field at the top or middle of the atmosphere, ground-based deployments obtain downwelling measurements of sky spectral diffuse radiance and irradiance together with the directly transmitted solar irradiance. The validation approach adopted for MISR consists of comparing geophysical parameters generated using MISR algorithms adapted to use with aircraft, MISR algorithms adapted to retrievals using the downwelling radiation field at the bottom-of-the-atmosphere, and using independent algorithms on ground-based observations in order to secure ground-based estimates of aerosol spectral optical depth, effective size distribution, phase function, and single scattering albedo. Validation of cloud parameters focus on the RLRA retrieval, using stereo imagery, accurate manual and automated stereo-photogrammetric techniques, and comparison with MISR algorithm results.

A comprehensive description of the MISR validation program is provided in [M-16].

#### 9.1.1 Aircraft instruments

Two aircraft instruments are used as MISR simulators as part of the validation program.

- (1) The Advanced Solid-State Array Spectrometer (ASAS) [59]. This instrument has flown on the C-130 and P3A aircraft platforms at altitudes of about 20000 feet above terrain generating a swath width of 1 - 2 km depending on flight altitude and a pixel size on the ground on the order of a few meters. ASAS views from 70° forward to 55° aftward. The spectral range is approximately 400 - 1000 nm represented by 62 channels each about 10 nm in bandwidth;
- (2) The Airborne MISR Simulator (AirMISR). This instrument flies aboard the ER-2 platform at an altitude of 65000 - 70000 feet above terrain. AirMISR is constructed from MISR brassboards, protoflight spares, and engineering models of actual MISR camera optics and electronics and in addition utilizes existing ground data systems. A single camera is pointed over the MISR view angle

range using a computer-controlled gimbal. The area seen in common at all angles is about 9 km x 11 km.

### **9.1.2 Field measurements**

Aircraft overflights are closely coordinated with the following ground-based observations:

- (1) Surface BRF of target areas at the MISR wavelengths using the PARABOLA (version III) sphere scanning radiometer (see [19] for description of earlier versions of PARABOLA);
- (2) Multispectral sky radiance, polarization and direct solar irradiance observations with Reagan sunphotometers and CIMEL sky and sunphotometers, and diffuse/direct irradiance measurements from a Yankee Environmental Systems (YES) multifilter rotating shadowband radiometer (MFRSR);
- (3) High spectral resolution (i.e., 10 nm between 390 and 2500 nm) determinations of optical depth using a Geophysical Environmental Research (GER) field spectrometer;
- (4) Vertical soundings of temperature and relative humidity using a balloon borne instrument package. Surface pressure and temperature, relative humidity (RH), wind speed and wind direction are continuously monitored using a Davis Meteorological Instrument package at the surface. Two conventional fish-eye lens camera systems can be deployed along a measured baseline to record cloud cover, cloud motion and cloud altitude.

## **9.2 QUALITY ASSESSMENT**

Having good data quality assessment (QA) is essential if the MISR data are to be scientifically meaningful to our users. The need for parts of the MISR QA activity to occur at each of three sites: (1) in the Product Generation System (PGS) software, (2) with the DAAC operator, and (3) at the Science Computing Facility (SCF).

### **9.2.1 Quality Assessment within the PGS software**

Routine QA processing will be automated. Human involvement will be limited to (1) spot checking of the data stream, and (2) investigating "anomalies." This puts most of the QA burden on the standard PGS software, which will create "indicators" of key aspects of the data quality and retrieval performance. PGS software QA indicator types include parameters describing instrument performance, processing paths, physical constraints, algorithmic constraints, climatological constraints, and external data sources. Some of the indicators will be designated as "alarms." These will be used for real-time QA of the MISR data stream. Further information on this type of quality assessment is found in [M-17].

### **9.2.2 Quality Assessment at the DAAC**

QA operations at the DAAC requiring human involvement will involve monitoring alarms, and possibly examining displays created by the real-time data stream. The operator will respond by recording anomalies in the QA Log, and contacting the SCF about the anomaly in a timely manner, for further action.

### **9.2.3 Quality Assessment at the SCF**

At the SCF, QA amounts to performing those tasks that require the attention of the MISR Instrument Team, Science Team, or Science Data System Team, and performing any processing steps that cannot be automated at the DAAC.

## 10. REFERENCES

- [1] Ahmad, S.P. and D.W. Deering (1992). A simple analytical function for bidirectional reflectance. *J. Geophys. Res.* **97**, 18,867-18,886.
- [2] Asrar, G., M. Fuchs, E.T. Kanemasu, and J.H. Hatfield (1984). Estimating absorbed photosynthetic radiation and leaf area index from spectral reflectance in wheat. *Agron. J.* **76**, 300-306.
- [3] Asrar, G., R.B. Myneni, and B.J. Choudhury (1992). Spatial heterogeneity in vegetation canopies and remote sensing of absorbed photosynthetically active radiation: A modelling study. *Remote Sens. Environ.* **41**, 85-103.
- [4] Baret, F. and G. Guyot (1991). Potential and limits of vegetation indices for LAI and APAR assessment. *Remote Sens. Environ.* **35**, 161-173.
- [5] Borel, C. C., S.A.W. Gerstl, and B.J. Powers, B. J. (1991). The radiosity method in optical remote sensing of structured 3-D surfaces. *Remote Sens. Environ.* **36**, 13-44.
- [6] Charlson, R. J., J. Lovelock, M. Andreae, and S. G. Warren (1987). Oceanic phytoplankton, atmospheric sulphur, cloud albedo and climate. *Nature* **326**, 655-661.
- [7] Charlson, R. J., J. Langner, H. Rodhe, C. B. Leovy, and S. G. Warren (1991). Perturbation of the northern hemispheric radiative balance by backscattering from anthropogenic sulfate aerosols. *Tellus* **43AB**, 152-163.
- [8] Charlson, R. J., S. Schwartz, J. Hales, R. Cess, J. Coakley, Jr., J. Hansen, J., and D. Hoffmann (1992). Climate forcing by anthropogenic aerosols. *Science* **255**, 423-430.
- [9] Charney, J., W.J. Quirk, S. Chow, and J. Kornfield (1977). A comparative study of the effects of albedo change on droughts in semi-arid regions, *J. Atmos. Sci.* **34**, 1366.
- [10] Choudhury, B. J., (1987). Relationship between vegetation indices, radiation absorption, and net photosynthesis evaluated by a sensitivity analysis. *Remote Sens. Environ.* **22**, 209-233.
- [11] Coakley, J. A. and F. P. Bretherton (1982). Cloud cover from high-resolution scanner data: Detecting and allowing for partially filled fields of view. *J. Geophys. Res.* **87**, 4917.
- [12] Coakley, J. A. and R. Davies (1986). The effect of cloud sides on reflected solar radiation as deduced from satellite observations. *J. Atmos. Sci.* **43**, 1025.
- [13] Coakley, J. A., R. L. Bernstein and P. D. Durkee (1987). Effects of ship effluents on cloud reflectivity. *Science* **237**, 1020.

- [14] Cox, C. and W. Munk (1954). Measurements of the roughness of the sea surface from photographs of the Sun's glitter. *Jour. Opt. Soc. of Am.* **44**, 838.
- [15] d'Almeida, G. A., P. Koepke, and E. P. Shettle (1991). Atmospheric Aerosols: Global climatology and radiative characteristics. Deepak Publishing.
- [16] Daughtry, C. S. T., K.P. Gallo, and M. E. Bauer (1983). Spectral estimates of solar radiation intercepted by corn canopies. *Agron. J.* **75**, 527-531.
- [17] Day, T., and Muller, J-P. (1989). Digital elevation model production by stereo-matching SPOT image-pairs: A comparison of algorithms. *Image and Vision Computing* **7**, 95.
- [18] Davies, R. (1984). Reflected solar radiances from broken cloud scenes and the interpretation of scanner measurements. *J. Geophys. Res.* **89**, 1259.
- [19] Deering, D.W., and P. Leone (1986). A sphere-scanning radiometer for rapid directional measurements of sky and ground, *Remote Sens. Environ.* **19**, 1.
- [20] Dickinson, R. E. (1981). Land surface processes and climate-Surface albedos and energy balance. *Adv. Geophys.* **25**, 305.
- [21] Dickinson, R. E., B. Pinty, and M.M. Verstraete (1990). Relating surface albedos in GCM to remotely sensed data. *Agric. and Forest Meteorol.* **52**, 109-131.
- [22] Di Girolamo, L. (1992). On the detection of cirrus clouds from satellite measurements. Master of Science thesis, Dept. of Meteorology, McGill Univ., Montreal, PQ.
- [23] Di Girolamo, L. and R. Davies (1994). A Band-Differenced Angular Signature technique for cirrus cloud detection. *IEEE Trans. Geosci. Rem. Sens.* **32**, 890-896.
- [24] Diner, D.J. and J.V. Martonchik (1984a). Atmospheric transfer of radiation above an inhomogeneous non-lambertian reflective ground. I. Theory. *J. Quant. Spect. Rad. Trans.* **31**, 97-125.
- [25] Diner, D.J. and J.V. Martonchik (1984b). Atmospheric transfer of radiation above an inhomogeneous non-lambertian reflective ground. II. Computational considerations and results. *J. Quant. Spect. Rad. Trans.* **32**, 279-304.
- [26] Diner, D. J. and J. V. Martonchik (1985). Atmospheric transmittance from spacecraft using multiple view angle imagery. *Appl. Opt.* **24**, 3503.
- [27] Ebert, E.E. (1987). A pattern recognition technique for distinguishing surface and cloud types in the polar regions. *J. Clim. Appl. Met.* **26**, 1412.

[28] Fraser, R. S. (1976). Satellite measurement of mass of Sahara dust in the atmosphere. *Appl. Opt.* **15**, 2471.

[29] Fraser, R. S. and Y. J. Kaufman (1985). The relative importance of aerosol scattering and absorption in remote sensing. *IEEE Trans. Geosci. and Rem. Sens.* **GE-23**, 625.

[30] Gallaudet, T.C. and J.J. Simpson (1991). Automated cloud screening of AVHRR imagery using split-and-merge clustering. *Remote Sens. Environ.* **38**, 77

[31] Gallo, K. P., C. S. T. Daughtry, and M.E. Bauer (1985). Spectral estimation of absorbed photosynthetically active radiation in corn canopies. *Remote Sens. Environ.* **17**, 221-232.

[32] Gerstl, S. A. W. and A. Zardecki (1985). Coupled atmosphere/canopy model for remote sensing of plant reflectance features. *Appl. Opt.* **24**, 94-103.

[33] Gerstl, S. A. W and C. Simmer (1986). Radiation physics and modeling for off-nadir satellite-sensing of non-lambertian surfaces. *Rem. Sens. Environ.* **20**, 1.

[34] Gerstl, S. A. W., C. Simmer, and B. J. Powers (1986). The canopy hot-spot as crop identifier. *Symposium on Remote Sensing for Resources Development and Environmental Management*, Enchede, 261.

[35] Gillespie, A. R. and A.B. Kahle (1977). Construction and interpretation of a digital thermal inertia image. *Photogramm. Eng. Remote Sens.* **43**, 983-999.

[36] Goel, N.S. and R.L. Thompson (1984). Inversion of vegetation canopy reflectance models for estimating agronomic variables. V. Estimation of leaf area index and average leaf angle using measured canopy reflectances. *Remote Sens. Environ.* **16**, 69.

[37] Goel, N. S., I. Rozehnal, and R.L. Thompson (1991). A computer graphics based model for scattering from objects of arbitrary shapes in the optical region. *Remote Sens. Environ.* **36**, 73-104.

[38] Goodman, A.H. and A. Henderson-Sellers (1988). Cloud detection analysis: A review of recent progress. *Atm. Res.* **21**, 203.

[39] Gordon, H. R. and D. K. Clark (1981). Clear water radiances for atmospheric correction of Coastal Zone Color Scanner imagery. *Appl. Opt.* **20**, 4175.

[40] Gordon, H. R., D. K. Clark, J. W. Brown, O. B. Brown, R. H. Evans and W. W. Broenkow (1983). Phytoplankton pigment concentrations in the Middle Atlantic Bight: Comparison of ship determinations and Coastal Zone Color Scanner measurements. *Appl. Opt.* **22**, 3929.

[41] Gordon H. R. (1984). Some studies of atmospheric optical variability in relation to



CZCS atmospheric correction (NOAA National Environmental Satellite and Data Information Service, Final Report Contract No. NA-79-SAC-00714).

[42] Gordon, H.R. and M. Wang (1994). Retrieval of water-leaving radiance and aerosol optical thickness over the oceans with SeaWiFS: A preliminary algorithm. *Appl. Opt.* **33**, 443-452 .

[43] Govaerts, Y. and M. M. Verstraete (1995). Evaluation of the capability of BRDF models to retrieve structural information on the observed target as described by a three-dimensional ray tracing code In *The European Symposium on Satellite Remote Sensing*, EUROPTO-SPIE Conference, Rome, 26-30 September 1994, *SPIE* **2314**, 9-20.

[44] Goward, S. N. and K.F. Huemmerich (1992). Vegetation canopy PAR absorptance and the normalized difference vegetation index: An assessment using the SAIL model. *Remote Sens. Environ.* **39**, 119-140.

[45] Griggs, M. (1975). Measurements of atmospheric aerosol optical thickness over water using ERTS-1 data. *J. Air Pollut. Control Assoc.* **25**, 622.

[46] Griggs, M. (1983). Satellite measurements of tropospheric aerosols. *Adv. Space Res.* **2**, 109.

[47] Gu, Z. Q., C. N. Duncan, E. Renshaw, M. A. Mufflstone, C. F. N. Cowan, P. M. Grant (1989). Comparison of techniques for measuring cloud texture in remotely sensed satellite meteorological image data. *IEE Proc.* **136**, 236.

[48] Gustafson, G.B., R.G. Isaacs, R.P. d'Entremont, J.M. Sparrow, T.M. Hamill, C. Grassotti, D.W. Johnson, C.P. Sarkisian, D.C. Peduzzi, B.T. Pearson, V.D. Jakabhazy, J.S. Belfiore, A.S. Lisa (1994). Support of Environmental Requirements for Cloud Analysis and Archive (SERCAA): algorithm descriptions. **PL-TR-94-2114**, Phillips Laboratory, AFMC, Hanscom AFB, MA.

[49] Hall, F. G., D. E. Strebel, S. J. Goetz, K. D. Woods and D. B. Botkin (1987). Landscape pattern and successional dynamics in the boreal forest. *Proceedings of the 1987 IGARSS Symposium*, **IEEE 87 CH2434-9**, 473.

[50] Hall, F. G., K.F. Huemmrich, S.J. Goetz, P.J. Sellers, and J.E. Nickeson (1992). Satellite remote sensing of surface energy balance: Success, failures, and unresolved issues in FIFE. *J. Geophys. Res.* **97**, 19,061-19,089.

[51] Hapke, B. (1981). Bidirectional reflectance spectroscopy. I. Theory. *J. Geophys. Res.* **86**, 3039-3054.

[52] Harshvardhan, R. Davies, D. A. Randall and T. G. Corsetti (1987). A fast radiation parameterization for atmospheric circulation models. *J. Geophys. Res.* **92**, 1009.

[53] Hasler, A. F. (1981). Stereographic observations from geosynchronous satellites: An important new tool for the atmospheric sciences. *Bull. Amer. Met. Soc.* **62**, 194.

[54] Hasler, A. F., R. Mack, and A. Negri (1983). Stereoscopic observations from meteorological satellites. *Adv. Space Res.* **2**, 105.

[55] Holben, B. N., D. Kimes and R. S. Fraser (1986) Directional reflectance response in AVHRR red and near-IR bands for three cover types and varying atmospheric conditions. *Rem. Sens. Environ.* **19**, 213.

[56] Husar, R.B., L.L. Stowe, and J. Prospero (1996). Patterns of tropospheric aerosols. Submitted to *Bull. Amer. Meteor. Soc.*

[57] Iaquina, J. and B. Pinty (1994). Adaptation of a bidirectional reflectance model including the hot-spot to an optically thin canopy. *Proceedings of the 6th ISPRS International Symposium on Physical Measurements and Signatures in Remote Sensing*, Val d'Isere, France, 17-21 January 1994, CNES, 683-690.

[58] Ignatov, A.M., L.L. Stowe, S.M. Sakerin, and G.K. Korotaev (1995). Validation of the NOAA/NESDIS satellite aerosol product over the north atlantic in 1989. *J. Geophys. Res.*, in press.

[59] Irons, J. R., K. J. Ranson, D. L. Williams, R. R. Irish, and F. G. Huegel (1991). An off-nadir-pointing imaging spectroradiometer for terrestrial ecosystem studies. *IEEE. Trans. Geosci. Rem. Sens.* **GE-29**, 66.

[60] Irvine, W. M. (1966). The shadowing effect in diffuse reflection. *J. Geophys. Res.* **71**, 2931-2937.

[61] Kahn, R., R. West, D. McDonald, B. Rheingans, and M.I. Mishchenko (1996). Sensitivity of multi-angle remote sensing observations to aerosol sphericity. Submitted to *J. Geophys. Res.*

[62] Kassander, A. R., Jr., and L. L. Simms (1957). Cloud photogrammetry with ground-located K-17 aerial cameras. *J. Meteorol.* **14**, 43.

[63] Kaufman, Y. J., and C. Sendra (1988). Algorithm for atmospheric corrections. *Int. J. Remote Sens.* **9**, 1357-1381.

[64] Kaufman, Y. J. (1989). The atmospheric effect in remote sensing and its correction. In *Theory and Applications of Optical Remote Sensing*, G. Asrar, ed., Wiley and Sons, 734 pp.

[65] Kiehl, J.T., and B.P. Briegleb (1993). The relative roles of sulfate aerosols and greenhouse gases in climate forcing. *Science* **260**, 311-314.

[66] Kimes, D. S. and J. A. Kirchner (1982). Radiative transfer model for heterogeneous 3D scenes. *Appl. Opt.* **21**, 4119-4129.

[67] Kimes, D. S. and P. J. Sellers (1985). Inferring hemispherical reflectance of the Earth's surface for global energy budgets from remotely sensed nadir or directional radiance values. *Rem. Sens. Environ.* **18**, 205.

[68] Kimes, D. S., P. J. Sellers and D. J. Diner (1987). Extraction of spectral hemispherical reflectance (albedo) of surfaces from nadir and directional reflectance data. *Int. J. Rem. Sens.* **8**, 1727.

[69] King, M. D., Y. J. Kaufman, W. P. Menzel, and D. Tanre (1992). Remote sensing of cloud, aerosol, and water vapor properties from the Moderate resolution Imaging Spectrometer (MODIS). *IEEE Trans. Geosci. Remote Sens.* **30**, 2-27.

[70] Knyazikhin, Y. V., A.L. Marshak, and R.B. Myneni (1992). Interaction of photons in a canopy of finite-dimensional leaves. *Remote Sens. Environ.* **39**, 61-74.

[71] Krekov, G. M. (1993). Models of atmospheric aerosols, in *Aerosol Effects on Climate*, S. G. Jennings, ed., University of Arizona Press, pp. 304.

[72] Lee, T. and Y. J. Kaufman (1986). The effect of surface nonlambertianity on remote sensing. *IEEE. Trans. Geosci. Remote Sens.* **GE-24**, 699-708.

[73] Li, X. and A.H. Strahler (1986). Geometric-optical bidirectional reflectance modeling of a conifer forest canopy. *IEEE Trans. Geosci. Remote Sens.* **24**, 906-919.

[74] Li, X. and A.H. Strahler (1992). Geometric-optical bidirectional reflectance modeling of the discrete crown vegetation canopy: Effect of crown shape and mutual shadowing. *IEEE Trans. Geosci. Remote Sens.* **30**, 276-292.

[75] Liang, S. and A.H. Strahler (1993). Calculation of the angular radiance distribution for a coupled atmosphere and canopy. *IEEE Trans. Geosci. Remote Sens.* **31**, 491-502.

[76] Long, C. S., and L. L. Stowe (1993). Using the NOAA/AVHRR to study stratospheric aerosol optical thickness following the Mt. Pinatubo eruption. *Geophys. Res. Lett.*, submitted.

[77] Lorenz, D. (1983). Stereoscopic imaging from polar orbit and synthetic stereo imaging. *Adv. Space Res.* **2**, 133.

[78] Los, S. O., C. O. Justice, and C. J. Tucker (1994). A global 1° x 1° NDVI data set for climate studies derived from the GIMMS continental NDVI data. *Int. J. Rem. Sens.* **15**, 3493-3518.

[79] Lumme, K. and E. Bowell (1981). Radiative transfer in the surfaces of atmosphereless

bodies. 1. Theory. *Astron. Jour.* **86**, 1694-1704.

[80] Marshak, A.L. (1989). The effect of the hot spot on the transport equation in plant canopies. *J. Quant. Spectrosc. Rad. Transf.* **42**, 615-630.

[81] Martonchik, J. V., and D. J. Diner (1992). Retrieval of aerosol optical properties from multi-angle satellite imagery. *IEEE Trans. Geosci. Rem. Sens.* **GE-30**, 223.

[82] Mekler, Y. and J. H. Joseph (1983). Direct determination of surface albedos from satellite imagery. *J. Clim. Appl. Meteorol.* **22**, 530.

[83] Minnaert, M. (1941). The reciprocity principle in lunar photometry. *Astrophys. Jour.* **93**, 403-410.

[84] Mintz, Y. (1984), *The Global Climate* (J.T. Houghton, ed.), Cambridge University Press, Cambridge, London, New York, 79-105.

[85] Muller, J-P. (1989). Real-time stereo matching and its role in future mapping systems. Survey & Mapping 89, University of Warwick, 17-21 April 1989, 15 pp.

[86] Myneni, R. B. and G. Asrar (1993). Radiative transfer in 3-Dimensional atmosphere vegetation media. *J. Quant. Spectrosc. Rad. Transf.* **49**, 585-598.

[87] Myneni, R. B., and D.L. Williams (1994). On the relationship between FAPAR and NDVI, *Remote Sens. Environ.* **49**, 200-211.

[88] Myneni, R. B., S. Maggion, J. Jaquinta, J.L. Privette, N. Gobron, B. Pinty, D.S. Kimes, M.M. Verstraete, and D.L. Williams (1995). Optical remote sensing of vegetation: Modeling, caveats, and algorithms. *Remote Sens. Environ.* **51**, 169-188.

[89] Nilson, T. and A. Kuusk (1989). A reflectance model for the homogeneous plant canopy and its inversion. *Remote Sens. Environ.* **27**, 157-167.

[90] Otterman, J. (1983). Absorption of insolation by land surfaces with sparse vertical protrusions. *Tellus* **35B**, 309-318.

[91] Peslen, C. A., S. E. Koch, and L. W. Uccellini (1985). The effect of arbitrary level assignment of satellite cloud motion wind vectors on wind analyses in the pre-thunderstorm environment. *NASA Tech. Memo 86186*, GSFC, 56 pp.

[92] Peterson, J. T., E. C. Flowers, G. J. Beni, C. L. Reynolds and J. H. Rudisill (1981). Atmospheric turbidity over central North Carolina. *J. Appl. Meteor.* **20**, 229.

[93] Pinty, B. and D. Ramond (1986). A simple bidirectional reflectance model for terrestrial

surfaces. *J. Geophys. Res.* **91**, 7803-7808.

[94] Pinty, B. and M. M. Verstraete (1991). Extracting information on surface properties from bidirectional reflectance measurements. *J. Geophys. Res.* **96**, 2865.

[95] Potter, C. S., J. T. Randerson, C. B. Field, P. A. Matson, P. M. Vitousek, H. A. Mooney, and S. A. Klooster (1993). Terrestrial ecosystem production: A process model based on global satellite and surface data. *Global Biogeochem. Cycles* **7**, 811-841.

[96] Powers, B.J. and S.A.W. Gerstl (1987). Modelling of atmospheric effects on the angular distribution of a backscattering peak. *Proc. IGARSS'87 Symposium* **1**, 635.

[97] Prince, S. D. (1991). A model of regional primary production for use with coarse resolution satellite data. *Int. J. Rem. Sens.* **12**, 1313-1330.

[98] Rahman, H., B. Pinty, and M.M. Verstraete (1993). Coupled Surface-Atmosphere Reflectance (CSAR) model. 2. Semiempirical surface model usable with NOAA Advanced Very High Resolution Radiometer data. *J. Geophys. Res.* **98**, 20,791-20,801.

[99] Rao, C. R. N., L. L. Stowe, and E. P. McClain (1989). Remote sensing of aerosols over the oceans using AVHRR data: Theory, practice and applications. *Int. J. Remote Sensing* **10**, 743.

[100] Roach, W. T. (1967). On the nature of the summit areas of severe storms in Oklahoma. *Quart. J. Roy. Meteorol. Soc.* **93**, 318.

[101] Ross, J. (1981). *The Radiation Regime and Architecture of Plant Stands*. W. Junk, Boston.

[102] Ross, J. and A.L. Marshak (1991). Monte Carlo methods. In *Photon-Vegetation Interactions*, R. Myneni and J. Ross, ed. Springer-Verlag, New York, 441-467.

[103] Rossow, W.B. (1989). Measuring cloud properties from space: A review. *J. Clim.* **2**, 201.

[104] Rossow, W.B., F. Moshier, E. Kinsella, A. Arking, M. Desbois, E. Harrison, P. Minnis, E. Ruprecht, G. Seze, C. Simmer, and E. Smit (1985). ISCCP cloud algorithm intercomparison. *J. Clim. Appl. Met.* **24**, 877.

[105] Roujean, J-L., M. Leroy, and P-Y. Deschamps (1992). A bidirectional reflectance model of the Earth's surface for the correction of remote sensing data. *J. Geophys. Res.* **97**, 20,455-20,468.

[106] Running, S. W., and J. C. Coughlan (1988). A general model of forest ecosystem processes for regional applications, I, Hydrological balance, canopy gas exchange and primary pro-

duction processes. *Ecol. Model.* **42**, 125-154.

[107] Schiffer, R. A. and W. B. Rossow (1983). The International Satellite Cloud Climatology Project (ISCCP): The First Project of the World Climate Research Program (WCRP). *Bull. Amer. Met. Soc.* **64**, 779.

[108] Sellers, P. J. (1985). Canopy reflectance, photosynthesis and transpiration. *Int. J. Rem. Sens.* **8**, 1335.

[109] Sellers, P. J. (1987). Canopy reflectance, photosynthesis and transpiration II: The role of biophysics in the linearity of their interdependence. *Rem. Sens. Env.* **21**, 143.

[110] Sellers, P. J., S. O. Los, C. J. Tucker, C. O. Justice, D. A. Dazlich, G. J. Collatz, and D. A. Randall (1994). A global  $1^\circ \times 1^\circ$  NDVI data set for climate studies. Part 2: The generation of global fields of terrestrial biophysical parameters from the NDVI. *Int. J. Rem. Sens.* **15**, 3519-3545.

[111] Shaw, G. E. (1982). Atmospheric turbidity in the polar regions. *J. Appl. Meteorol.* **21**, 1080.

[112] Shenk, W. E., R. J. Holub, and R. A. Neff (1975). Stereographic cloud analysis from Apollo-6 photographs over a cold front. *Bull. Am. Meteorol. Soc.* **56**, 4.

[113] Shettle, E.P. and R.W. Fenn (1979). Models for the aerosols of the lower atmosphere and the effects of humidity variations on their optical properties. Air Force Geophysics Laboratory, Hanscomb AFB, MA 01731, AFGL-TR-79-0214.

[114] Shultis, J. K. and R.B. Myneni (1988). Radiative transfer in vegetation canopies with anisotropic scattering. *J. Quant. Spectrosc. Rad. Transf.* **39**, 115-129.

[115] Slater, P. N. and R. D. Jackson (1982). Atmospheric effects on radiation reflected from soil and vegetation as measured by orbital sensors using various scanning directions. *Appl. Opt.* **21**, 3923-3931.

[116] Slater, P. and L. Mendenhall (1993). *Proceedings of the Workshop on Atmospheric Correction of Landsat Imagery*. Sponsored by the Defense Landsat Program Office, Torrance, CA, 233 pp.

[117] Smith, G. L., R. N. Green, E. Raschke, L. M. Avis, J. T. Suttles, B. A. Wielicki, and R. Davies (1986). Inversion methods for satellite studies of the Earth's radiation budget: Development of algorithms for the ERBE mission. *Rev. Geophys.* **24**, 407.

[118] Stephens, G., and S-C. Tsay (1990). On the cloud absorption anomaly. *Qrtly. J. Royal*

*Meteorol. Soc.* **116**, 671-704.

[119] Stowe, L. L., R. M. Carey, and P. P. Pellegrino (1992). Monitoring the Mt. Pinatubo aerosol layer with NOAA/11 AVHRR data. *Geophys. Res. Lett.* **19**, 159-162.

[120] Suttles, J. T., and G. Ohring (1986). Workshop on surface radiation budget for climate applications. World Climate Research Program, WCP-115, WMO/TD-No. 109, Columbia, Md., 18-21 June 1985.

[121] Tanre, D. M. Herman, and P. Y. Deschamps (1981). Influence of the background contribution upon space measurements of ground reflectance. *Appl. Opt.* **20**, 3676-3684.

[122] Taylor, V. R. and L. L. Stowe (1984). Reflectance characteristics of uniform Earth and cloud surfaces derived from Nimbus-7 ERB. *J. Geophys. Res.* **89**, 4987.

[123] Toon, O. B. and J. B. Pollack (1976). A global average model of atmospheric aerosols for radiative transfer calculations. *J. Appl. Meteor.* **15**, 225.

[124] Tovinkere, V.R., M. Penaloza, A. Logar, J. Lee, R.C. Weger, T.A. Berendes, and R.M. Welch (1993). An intercomparison of artificial intelligence approaches for polar scene identification. *J. Geophys. Res.* **98**, 5001.

[125] Tucker, C. J. (1979). Red and photographic infrared linear combinations for monitoring vegetation. *Remote Sens. Environ.* **8**, 127-150.

[126] Turco, R. P., R.C. Whitten, and O. B. Toon (1982). Stratospheric aerosols: Observation and theory. *Rev. Geophys. Space Phys.* **20**, 233-279.

[127] Twomey, S. (1977). The influence of pollution on the shortwave albedo of clouds. *J. Atmos. Sci.* **34**, 1149.

[128] Valero, F. P. J. and T. P. Ackerman (1986). Arctic haze and the radiation budget. In *Arctic Air Pollution*, B. Stonehouse, Ed. Cambridge University Press, Cambridge.

[129] Vali, G., ed., (1991). Report of the Experts Meeting on Interaction Between Aerosols and Clouds. WCRP-59, WMO / TD-No. 423.

[130] Verstraete, M. M., B. Pinty, and R.E. Dickinson (1990). A physical model of the bidirectional reflectance of vegetation canopies. 1. Theory. *J. Geophys. Res.* **95**, 11,775-11,765.

[131] Wanner, W., Li, X., and A.H. Strahler (1995). On the derivation of kernels for kernel-driven models of bidirectional reflectance. *J. Geophys. Res.* **100**, 21,077-21,089.

[132] Welch, R. M. and Wielicki, B. A. (1984). Stratocumulus cloud field reflected fluxes:

The effect of cloud shape. *J. Atmos. Sci.* **41**, 3085.

[133] Welch, R.M., Sengupta, S.K. and D.W. Chen (1988). Cloud field classification based upon high spatial resolution textural features. 1. Gray level co-occurrence matrix approach. *J. Geophys. Res.* **93**, 12663.

[134] Whitehead, V. S., I. D. Browne, and J. G. Garcia (1969). Cloud height contouring from Apollo-6 photography. *Bull. Am. Meteorol. Soc.* **50**, 522.

[135] Wiegand, C. L., A.J. Richardson, D.E. Escobar, and A. H. Gerbermann (1991). Vegetation indices in crop assessments. *Remote Sens. Environ.* **35**, 105-119.

[136] Wielicki, B. A. and L. Parker (1992). On the determination of cloud cover from satellite sensors: The effect of sensor spatial resolution. *J. Geophys. Res.* **97**, 12,799-12,823.

[137] Williamson, S. J. (1972). Fundamentals of Air Pollution. Addison-Wesley, MA.

[138] World Climate Programme WCP-112 (1984). A Preliminary Cloudless Standard Atmosphere for Radiation Computation. IAMAP (International Association for Meteorology and Atmospheric Physics), Boulder, CO, pp.53.